NASA/TM-20205008519

1- by 1-Foot Supersonic Wind Tunnel Sidewall Flowfield Compression Plate Study

Christopher J. Peters, Christine M. Pastor-Barsi, and David O. Davis
Glenn Research Center, Cleveland, Ohio

November 2020

NASA STI Program . . . in Profile

Since its founding, NASA has been dedicated to the advancement of aeronautics and space science. The NASA Scientific and Technical Information (STI) Program plays a key part in helping NASA maintain this important role.

The NASA STI Program operates under the auspices of the Agency Chief Information Officer. It collects, organizes, provides for archiving, and disseminates NASA's STI. The NASA STI Program provides access to the NASA Technical Report Server—Registered (NTRS Reg) and NASA Technical Report Server—Public (NTRS) thus providing one of the largest collections of aeronautical and space science STI in the world. Results are published in both non-NASA channels and by NASA in the NASA STI Report Series, which includes the following report types:

- TECHNICAL PUBLICATION. Reports of completed research or a major significant phase of research that present the results of NASA programs and include extensive data or theoretical analysis. Includes compilations of significant scientific and technical data and information deemed to be of continuing reference value. NASA counter-part of peer-reviewed formal professional papers, but has less stringent limitations on manuscript length and extent of graphic presentations.

- TECHNICAL MEMORANDUM. Scientific and technical findings that are preliminary or of specialized interest, e.g., "quick-release" reports, working papers, and bibliographies that contain minimal annotation. Does not contain extensive analysis.

- CONTRACTOR REPORT. Scientific and technical findings by NASA-sponsored contractors and grantees.

- CONFERENCE PUBLICATION. Collected papers from scientific and technical conferences, symposia, seminars, or other meetings sponsored or co-sponsored by NASA.

- SPECIAL PUBLICATION. Scientific, technical, or historical information from NASA programs, projects, and missions, often concerned with subjects having substantial public interest.

- TECHNICAL TRANSLATION. English-language translations of foreign scientific and technical material pertinent to NASA's mission.

For more information about the NASA STI program, see the following:

- Access the NASA STI program home page at http://www.sti.nasa.gov

- E-mail your question to help@sti.nasa.gov

- Fax your question to the NASA STI Information Desk at 757-864-6500

- Telephone the NASA STI Information Desk at 757-864-9658

- Write to:
  NASA STI Program
  Mail Stop 148
  NASA Langley Research Center
  Hampton, VA 23681-2199

NASA/TM-20205008519

1- by 1-Foot Supersonic Wind Tunnel Sidewall Flowfield Compression Plate Study

Christopher J. Peters, Christine M. Pastor-Barsi, and David O. Davis
Glenn Research Center, Cleveland, Ohio

National Aeronautics and
Space Administration

Glenn Research Center
Cleveland, Ohio 44135

November 2020

Acknowledgments

The authors would like to thank the many people who contributed to the success of this effort: Celia R. Otero, Brent T. Seifert, Jonathan R. Borman, Brian S. Rouse, Robert C. Clark, Mitchell J. Davic, Erhard S. Hartman, John M. Lucero and Gwynn A. Severt for their support of testing in NASA's 1x1 SWT; Chip Redding, David A. Gubics and Paul A. Solano for design and engineering of test hardware and instrumentation; Richard A. Kelsch and Timothy A. Dunlap for fabrication of test hardware and instrumentation; J. David Saunders and David W. Witte for originating the sidewall flowfield compression concept and preliminary investigations into its use, which stemmed from an earlier, two-page white paper by Randall T. Voland of ACEnT Laboratories. Heath H. Reising and David W. Witte served as technical reviewers of the manuscript. NASA's Hypersonic Technology Project (HTP) funded this work.

This work was sponsored by the Advanced Air Vehicle Program
at the NASA Glenn Research Center.

Level of Review: This material has been technically reviewed by technical management.

Available from

NASA STI Program
Mail Stop 148
NASA Langley Research Center
Hampton, VA 23681-2199

National Technical Information Service
5285 Port Royal Road
Springfield, VA 22161
703-605-6000

This report is available in electronic form at http://www.sti.nasa.gov/ and http://ntrs.nasa.gov/

1- by 1-Foot Supersonic Wind Tunnel Sidewall Flowfield Compression Plate Study

Christopher J. Peters, Christine M. Pastor-Barsi, and David O. Davis
National Aeronautics and Space Administration
Glenn Research Center
Cleveland, Ohio 44135

Abstract

A method for locally increasing the dynamic pressure in the test section of a supersonic wind tunnel is investigated from a theoretical, computational and experimental perspective, culminating in a reduced-scale, proof-of-concept test at Mach 3.44. Symmetric, variable-angle compression plates along the test section sidewalls generate oblique shockwaves to elevate the test section dynamic pressure (q). The experimental effort utilizes boundary-layer pitot rakes to sample the incoming flow near the floor, pitot and static rakes to measure the high-q core flow and numerous surface taps to map out the static pressure distribution along the floor, ceiling and sidewalls. A reliable and robust starting procedure is developed to establish supersonic flow in the test section and behind the compression plates. A characterization of the incoming floor boundary layer reveals previously documented features (such as a bulge toward the centerline) and an unexpected (and as-yet-unexplained) thickening of the boundary layer with increasing Reynolds number around total pressures of 40–60 psia. The high-q core flow is characterized for eight compression plate angles (4.0–8.0°), eight tunnel total pressures (20–139 psia) and three axial stations (24.95–27.35 inches). The peak dynamic pressure rise exceeds expectations. At conditions relevant to full-scale testing (6.0° and 139 psia), the dynamic pressure increases by a factor of 1.73, the Mach number becomes 2.85 and the total pressure drops imperceptibly. Basic distortion metrics show transverse non-uniformity of less than 5 %. Limited spatial resolution in the static rake measurements warrants additional, higher fidelity testing or computational analysis. Surface-mounted, fast-response instrumentation suggests minimal unsteadiness in the flow, less than a few percent of the mean (comparable to the sensor accuracy).

Nomenclature

Symbols

d = spanwise distance from CP leading edge to sidewall
h = test section height, 12.0 inches
M = Mach number
p = pressure
q = dynamic pressure, $\frac{1}{2}\rho u^2$
Re = Reynolds number
u = streamwise velocity
w = test section width, 12.2 inches
x = axial distance from nozzle exit plane (downstream is positive)
y = transverse distance from centerline (ceiling is positive)
y' = normal distance above floor surface
z = spanwise distance from centerline (port is positive)

Greek Symbols

α = compression plate ramp angle

δ = boundary-layer 99-percent thickness
δ^* = boundary-layer displacement thickness
θ = boundary-layer momentum thickness
ρ = density

Subscripts
0 = total (stagnation) condition
1 = pertaining to Zone 1 (Fig. 1)
2 = pertaining to Zone 2 (Fig. 1)
3 = pertaining to Zone 3 (Fig. 1)

I. Introduction

Compression plates (CPs) have been used previously to extend the operational envelope of supersonic flow facilities at NASA Glenn Research Center (GRC) [1, 2]. The present work seeks to evaluate a method of raising the dynamic pressure delivered to a model in the test section of a supersonic wind tunnel. Dynamic pressure is defined in the incompressible sense, $q = \frac{1}{2}\rho u^2$, where ρ represents static density and u denotes streamwise velocity. As shown in Fig. 1, symmetrically-opposed, variable-geometry compression plates generate oblique crossing/refracting shockwaves (red lines), resulting in a region of uniform, axial compressed flow (Zone 3) of elevated dynamic pressure (or high-q) and reduced Mach number. For a given Mach number in Zone 1, the amount of compression depends upon the ramp angle, α, of the plates. Relative to the incoming conditions in Zone 1, the oblique shockwaves increase the density, ρ, more than decreasing the velocity, u, ultimately producing a higher dynamic pressure, q, in Zone 3. The usable region of compressed flow in Zone 3 takes on the shape of a "kite," bounded by the refracted shockwaves (red lines) and the leading expansion waves (blue lines) generated at the trailing edges of the compression plates. The spatial extent of the kite and its position (i.e., position of the refraction point) depend upon the CP angle, shrinking and moving upstream with increasing α.[*] The pre-test design and engineering effort [3] optimized the geometric parameters (shown in Fig. 1) to maximize the test kite's size, ensure its desired placement and achieve sufficient dynamic pressure rise.

There are two primary concerns with this experimental approach to increasing dynamic pressure: wind tunnel blockage and flow uniformity/quality in the high-q region. The first concern results from increases to the effective blockage area in the wind tunnel from geometric and aerodynamic sources. Geometric blockage is associated with the projected area of the compression plate hardware and increases with α. Aerodynamic blockage is associated with the constricted flow between the plates and sidewalls, and the boundary-layer growth caused by multiple shockwave/boundary-layer interactions (SWBLIs). Excessive blockage can prevent a wind tunnel from starting [4] and/or maintaining steady supersonic flow. The second concern arises from non-ideal effects which may compromise the core flow. Although the inviscid portrayal in Fig. 1 shows uniform, axial high-q flow in Zone 3, viscous effects near the CPs and tunnel surfaces can significantly alter the flowfield. In particular, the glancing/crossing SWBLIs on the floor and ceiling can cause flow separation that will distort the core flow. This distortion may be exacerbated by the counter-rotating vortex pairs that develop along the non-contoured floor and ceiling of the facility's two-dimensional nozzle [5, 6].

Accordingly, the present study seeks to test a proof of concept at reduced scale in the 1- by 1-Foot Supersonic Wind Tunnel (1x1 SWT) at NASA GRC. Test conditions will have relevance to high-speed propulsion testing in the larger scale 10- by 10-Foot Supersonic Wind Tunnel (10x10 SWT) also at NASA GRC. The test intends to address the above concerns, demonstrating the ability of the tunnel to start (and remain started) at the desired operating conditions and the sidewall compression method to produce high-q flow of sufficient quality.

II. Summary of Previous Work

Utilization of crossing shocks of equal or unequal strength to manipulate flowfields is prevalent in the experimental fluid dynamics community. Generally speaking, there have been two types of approaches: model-mounted shock generators and facility-mounted shock generators.

Model-mounted shock generators are typically used in inlet experiments and are less likely to cause SWBLIs within the area of interest due to the particular nature of their implementation. Researchers at NASA GRC (formerly the NACA

---

[*] The spatial extent of the kite also depends on the CP length, but that parameter is fixed to 14.000 inches in this study.

Lewis Flight Propulsion Laboratory) have performed several studies which use oblique shockwaves or expansion fans to regulate the supersonic flow ingested by an inlet [1, 7]. Fox [1] adjusted the angle of a single flat plate to continuously vary the effective freestream Mach number (from 1.72 to 2.18) of a nominally fixed Mach 1.91 facility. Shown in Fig. 2(a), the suspended flat plate attached to the model hardware and varied the Mach number supplied to a series of inlets in the NACA Lewis 18- by 18-Inch Supersonic Wind Tunnel. Similarly, Hearth et al. [7] used an inclined plate directly attached to the model hardware to expand the flow, thereby extending the upper limit of the NACA Lewis 8- by 6-Foot Supersonic Wind Tunnel and providing some Mach variability (Mach 2.10 and 2.16) for ramjet testing. This setup is diagrammatically shown in Fig. 2(b). Overall, the model-mounted technique is effective for localized manipulation of the flow; however, when a larger volume of the flowfield needs altering, larger scale shock generators are required.

NASA GRC personnel have also performed several studies employing facility-mounted shock generators [2, 8–10]. As seen in Fig. 3(a), Hearth et al. [2] employed symmetric Mach (i.e., compression) plates to lower the operational limit of the 10x10 SWT down to Mach 1.8. Porcher et al. [8] later reported on this same study, framed in the context of B-58 inlet testing. Hingst et al. [9, 10] installed shock generators in the 1x1 SWT as shown in Fig. 3(b) to investigate the interaction of glancing, crossing shockwaves with a turbulent boundary layer at Mach 2.5–4.0. Reddy [11] compared these 1x1 SWT results to Navier-Stokes solutions obtained by a three-dimensional computational fluid dynamics (CFD) code. Observe that the mounting orientation in these experiments (i.e., along the test section floor and ceiling) is rotated with respect to the mounting orientation of the present study (i.e., along the test section sidewalls).

Davis et al. [5] more recently utilized experimental hardware similar to the present approach to investigate shockwave interaction with a turbulent boundary layer. The experiment showed that the distance from the shock crossing location to the trailing edge expansion off the compression plate must be greater than the incoming boundary-layer thickness to suppress the upstream influence of the expansion affecting the interaction region. Both Davis et al. [5] and Hingst et al. [9, 10] performed their experiments in the 1x1 SWT, the facility used in the present study. However, the shockwaves generated from the plates in those experiments intersected the sidewall boundary layers, while in the current experiment, the shockwaves intersect the floor and ceiling boundary layers. Figure 4 illustrates the boundary-layer Mach contours in the 1x1 SWT as surveyed by Davis et al. [5]. Figure 4(a) is taken directly from the report [5] and shows that the shock generators from that experiment are much closer to the centerline of the tunnel and interact with flat boundary-layer Mach contours. Figure 4(b) is adapted from the report [5] to show that the compression plates of the current setup are much closer to the sidewalls of the facility and interact with curved boundary-layer Mach contours instead of flat ones. Moreover, the boundary layer bulges towards the centerline where the shockwaves cross and refract. Interaction with this irregular and considerably thicker boundary layer likely exacerbates the SWBLI effects and associated flow distortion. Table 1 summarizes experiments in the 1x1 SWT comparable to the present study.

Table 1 Summary of selected experiments in the 1x1 SWT.

References	Mach number	Reynolds number (*h* or *w* basis)	Plate length, inch	Plate angle, deg
[9, 10]	3.48^a	4.45×10^6, *h*	7.99	4.0–12.0
[5]	3.44	4.6×10^6, *h*	9.00, 10.00	2.0–10.0, 2.0–9.0
Present study	3.44	$(2.6\text{–}19.6) \times 10^6$, *w*	14.00	2.0, 4.0–8.0

[a] Omitted data at Mach 2.47, 2.97 and 3.98 for brevity.

III. Pre-Test Predictions

A. Inviscid Flow Theory Predictions

Elementary inviscid flow theory [12, 13] facilitates analysis of the ideal performance of the sidewall compression method. Figure 5 plots ratios of downstream (Zone 3) to upstream (Zone 1) dynamic pressure, q_3/q_1, total pressure, p_{03}/p_{01}, and Mach number, M_3/M_1, calculated for different compression plate angles, α, and incoming Mach numbers, M_1. Note the relatively large gain in dynamic pressure for relatively small losses in total pressure and Mach number. At the design condition ($M_1 = 3.44$, $\alpha = 6.0°$), $q_3/q_1 = 1.70$, $p_{03}/p_{01} = 97.8\,\%$ and $M_3/M_1 = 80.8\,\%$. For constant M_1, increasing the compression plate angle magnifies the method's effect (enhancing dynamic pressure, but decreasing total pressure recovery and resultant Mach number). For constant compression plate angle, increasing M_1 similarly magnifies the effects to q_3/q_1 and p_{03}/p_{01}, but non-monotonically affects M_3/M_1. Furthermore, the value of M_1 which maximizes the ratio M_3/M_1 also depends on compression plate angle, ranging from $M_1 = 2.73$ for $\alpha = 2.0°$ to $M_1 = 2.97$ for $\alpha = 8.0°$.

B. Computational Fluid Dynamics Predictions

Pre-test computational fluid dynamics analysis was performed using the SolidWorks Flow Simulation tool. The goals of the analysis were to: 1) establish a qualitative assessment of the flow quality within the test kite accounting for viscous and SWBLI effects, 2) build confidence that the flow passage between the sidewall and the backside of the compression plate can be started, and 3) for the purpose of hardware stress analysis, estimate: i) the loads on the compression plates when the flow is unstarted behind the plates, and ii) the dynamic pressure acting on a notional model located downstream of the test kite.

SolidWorks Flow Simulation is a commercial, user-friendly, Reynolds-averaged Navier-Stokes (RANS) flow solver that allows for medium-fidelity solutions using the software's default settings. The grid is generated directly from the three-dimensional solid model. For the simulations, the wind tunnel nozzle was not modeled, rather the test section was extended upstream to a location where a uniform inflow condition would yield a Mach number and boundary-layer thickness that closely matched the experimental conditions near the leading edge of the compression plates. However, by not modeling the nozzle, the aforementioned vortex pairs that develop along the floor and ceiling were not captured in the simulations. Compared to the experiment, the absence of the floor and ceiling vortex pairs likely improves the flow quality within the simulated test kite.

For the simulations, a dump diffuser was added onto the end of the test section with the outflow plane set at a near-vacuum condition. The floor, ceiling and sidewalls of the diffuser were set to a slip condition to minimize computational time. The entire flowfield was initialized at a Mach 3.5 condition with pressure and temperature in agreement with expected tunnel conditions.

A formal grid sensitivity study was not performed, but the typical approach was to start with the coarsest "automatic" grid, and then once converged, restart solution on the next finer grid until the finest automatic grid had converged. There was typically no discernible difference in the solution between the last and next-to-last grids.

With regard to flow quality, the results for the $\alpha = 6.0°$ and $\alpha = 8.5°$ cases are shown in Figs. 6 and 7, respectively. The upper plots show plan-view centerline Mach number contours. The inviscid shock and leading expansion wave are also indicated in the plots. For the $\alpha = 6.0°$ case, the inviscid shock and expansion agree well with the viscous calculations. For the $\alpha = 8.5°$ case, the initial shock is at a slightly steeper angle than the inviscid system, but still agrees fairly well. The lower plots in the figures are isometric views highlighting the flow distribution at the notional capture plane which is indicated by a black box drawn on the plane. For the $\alpha = 6.0°$ case, the flow entering the notional capture is fairly uniform. The floor SWBLI creates a mild compression followed by an expansion. The effect of the expansion is a slightly higher Mach number in the region nearest the floor. For the $\alpha = 8.5°$ case, similar, but more pronounced, results are shown.

The CFD approach to the compression plate backside starting concern was to show that if the flowfield was initialized to a started condition, then it would remain started after solution convergence. Steady-state RANS CFD is not particularly useful for predicting wind tunnel starting characteristics; however, if a started solution unstarts during the convergence process, it strongly suggests that starting problems will be encountered during the test. Ultimately though, experience and historical data must be considered to have adequate confidence in the "startability" of a hardware configuration. As reported by Davis [3], CFD analysis showed that the original design for the compression plate pivots would not be conducive to starting the flow behind the plates. It was always anticipated that compression plate angles of approximately 4–6° would be required to start the backside of the plates, but it was also desirable for the plates to remain started when brought down to 2° after starting at the higher angles. Since the CFD analysis started with the entire flowfield at Mach 3.5, the approach was to run the solution to convergence, and if it remained started, then there could be confidence that the configuration would start in the actual wind tunnel. Inasmuch as the startability improved with grid refinement, so long as a grid resulted in a started condition, it was considered an acceptable configuration. As a result of the CFD analysis, the pivot locations were moved from the sidewalls to the ceiling and floor, greatly opening up the flow passage behind the plates as shown in Fig. 8(a). Mach contours for the modified configuration are depicted in Fig. 8(b) and clearly show the backside of the plate is started at Mach 3.5 and $\alpha = 2.0°$.

IV. Experimental Setup, Test Configuration and Procedure

A. 1x1 SWT Facility (with Comparison to 10x10 SWT)

The 1- by 1-Foot Supersonic Wind Tunnel [14] is a continuous flow facility that provides a range of discrete Mach numbers (1.3 to 6.0) by employing interchangeable two-dimensional nozzles or Mach blocks. The nozzle sidewalls are contoured to provide gasdynamic expansion, similar to the 10- by 10-Foot Supersonic Wind Tunnel [15], although that larger facility utilizes a single nozzle with flexible sidewalls. For this study, the test section is $w = 12.2$ inches wide by $h = 12.0$ inches high and approximately 53.3 inches long. Thus, the 1x1 SWT can be thought of as a one-tenth-scale version of the 10x10 SWT since it has a square test section and a two-dimensional nozzle in the same orientation. Also, the present study uses the Mach 3.5 block (nominal effective Mach number of $M_1 = 3.44$), which corresponds to the upper operating limit of the 10x10 SWT. Compressors located at a remote site deliver combustion air (CA) service (40 or 150 psig) to the facility to accommodate the desired operating pressures and mass flow demands. Coarse and fine control valves regulate the supply pressure down to the desired plenum (total) pressure for the test. The air is clean and dry (dew point below 428 °R). Using higher total pressures, the 1x1 SWT can achieve similar test section Reynolds numbers (width basis) as the 10x10 SWT ($Re \approx 17\text{–}20 \times 10^6$) [3].

Figure 9 plots representative values of the incoming freestream Mach number, M_1, Reynolds number, Re_1, dynamic pressure, q_1, and total temperature, T_{01}, as a function of total pressure, p_{01} (i.e., the set point for testing in the 1x1 SWT). These data were acquired using configuration 9 of Table 3. As expected, Reynolds number and dynamic pressure scale linearly with total pressure. During a run, the variation in Mach number and total temperature was minimal, a few percent over each CA service range shown in the figure (20–50 psia and 50–141 psia, respectively). Across runs, however, the Reynolds number sometimes differed from the values shown in Fig. 9 by as much as 12 %, but typically 3.8 %, due to run-to-run or day-to-day variation of the total temperature[†] of the combustion air supply. This run-to-run variation was thought to be small enough to insignificantly affect the observed trends. The changeover in combustion air service occurs at $p_{01} = 50$ psia, with the 40 psig service providing finer, more stable control of the set point at the lower pressures. For these two runs, Fig. 9 shows only a slight jump in total temperature at the changeover.

B. Facility Data Acquisition

The majority[‡] of data presented herein were collected by Escort D, a “steady-state” data acquisition system developed by NASA GRC. Escort D obtains pressure readings from the electronically scanned pressure (ESP) system, sampling flexible pneumatic connections to the test section and rakes at a rate of 1 Hz for 12 seconds (the acquisition length chosen for this experiment). By relying on hourly self-calibrations, the system can achieve an overall accuracy of ±0.05 % of a module’s range. 15-, 45- and 100-pound-per-square-inch ESP modules were used, matched to the pressure ranges expected by the instrumentation. “Dynamic” data were acquired by high-bandwidth differential signal amplifiers (Dewetron MDAQ-BASE-5A) and analog-to-digital converter boards (Dewetron ORION-1624-200), sampling at a rate of 20 kHz for approximately 16 seconds. A 10 kHz low-pass filter suppressed signal aliasing. This dynamic data system was electrically connected to surface-mounted, fast-response sensors (Kulite® XCQ-062-25A ultra-miniature pressure transducer), with typical accuracy of ±0.1 % of range (25 psia), according to the manufacturer. These sensors were ‘calibrated’ in situ using the atmospheric and vacuum tares that occurred every time the tunnel was brought up to or taken down from operating conditions.

In this report, unless otherwise stated, markers and error bars respectively correspond to the arithmetic mean and sample standard deviation of the 12-second data acquisitions.

C. Test Hardware and Instrumentation

1. Compression Plates

Early designs of the compression plates strove to confine all hardware and associated mounting to the wind tunnel sidewalls. While wind tunnel blockage is one of the two primary concerns being investigated in this experiment, blockage on both sides of the compression plate was considered. As compression plate design progressed, to reduce blockage behind the plates, the forward pivots were relocated to the floor and ceiling as shown in Fig. 8(a) and described in Sec. III.B. Simulated Mach contours of the modified configuration are depicted in Fig. 8(b) and clearly show supersonic

---

[†] T_{01} sometimes differed from the values shown in Fig. 9 by as much as 6.6 %, but typically 2.3 %.

[‡] Every data figure, except Fig. 39 in Sec. V.F, relied on steady-state measurements from Escort D.

flow behind the plates at the expected tunnel starting condition of Mach 3.5 and $\alpha = 2.0°$. To retain stiffness, the plate thickness was increased by 0.125 inches to a final design thickness of 0.375 inches. After installation in the wind tunnel, a coordinate measuring machine or CMM (FaroArm® Edge, 9-foot, standard 7-axis) calibrated the plate actuation system and confirmed its ability to provide ramp angles[§] within ±0.05° of the desired value. The nominal compression plate design dimensions for the 1x1 SWT are shown in Fig. 1.

2. Rake Hardware

Figure 10 shows the measurement locations (denoted as asterisks) available for the upstream and downstream rakes with respect to the predicted evolution of the test kite. The upstream boundary-layer rakes had three spanwise locations (centerline and two port offsets) at a fixed axial station of 5.250 inches. The downstream high-q rakes had three spanwise locations (port, centerline and starboard) each with three axial stations (forward = 24.949 inches, mid = 26.149 inches, and aft = 27.349 inches). Note the placement of the downstream rakes versus the evolution of the refracted shock and expansion fan as a function of compression plate angle in Figs. 10(a) through 10(c).

The three upstream boundary-layer rakes are pictured in Fig. 11. Each rake has eleven pitot probes (spaced according to Table 2) and one base static. The port offsets from the centerline are 2.500 and 4.240 inches, respectively. These rakes were intended to measure the incoming boundary layer on both the floor and, when the test section plate is rotated, the sidewall. Due to testing constraints, only the floor boundary-layer data were collected and reported as part of this test entry.

Table 2 Probe spacing for upstream boundary-layer rake.

Pitot probe	1	2	3	4	5	6	7	8	9	10	11
y', inch	0.036	0.109	0.218	0.364	0.545	0.764	1.018	1.309	1.636	2.000	2.400
y'/h, %	0.3	0.9	1.8	3.0	4.5	6.4	8.5	10.9	13.6	16.7	20.0

The downstream port, centerline, and starboard pitot rakes are pictured in Fig. 12. The port and starboard positions are 1.200 inches off centerline in the positive and negative directions, respectively. Each pitot rake has sixteen probes and one base static tap. The rakes were designed to measure eight inches of the twelve-inch plane of interest at half-inch increments. Davis [3] elaborates on the design methodology of the rakes and the vertical extent of the notional capture.

The downstream static rake is pictured in Fig. 13. The rake has five conical probes,[¶] plus one base static pressure tap. The static rake was designed to measure eight inches of the twelve-inch plane of interest at two-inch increments (matching the pitot measurements at heights of 1.632, 3.632, 5.632, 7.632, and 9.632 inches).

3. Surface Pressure Taps

The surface static taps are placed to avoid regions of hardware mounting and actuation. Due to the complexity of the hardware/model mounting and the desire to have pressure taps on all four surfaces of the test section, it was not possible to utilize the facility schlieren windows. Locations of the static taps are shown in Fig. 14. Ceiling centerline statics are located 5.200 to 23.200 inches from tunnel datum (nozzle exit plane) while floor centerline statics are 9.200 to 21.200 inches (to accommodate the upstream and downstream rakes). Both the ceiling and floor plates have port and starboard statics 3.000 inches off of centerline, beginning at 25.200 inches from tunnel datum.

D. Test Configurations and Approach/Matrix

The test approach involved only the compression plate hardware, with flowfield measurements in lieu of a representative model or test article. This approach was used for the following reasons:

1) Map the test kite extent as a function of CP angle (4.0–8.0°),
2) Survey the test kite flowfield,
3) Determine the best model position with respect to the CPs for testing.

Table 3 lists the test configurations and tunnel total pressures used in the experiment. In the p_{01} column, the lower pressure sweep of 20, 27, 38 and 50 psia used 40 psig CA while the upper pressure sweep of 70, 90, 115 and 139 psia

---

[§] α was measured with respect to each sidewall as shown in Fig. 1.

[¶] Due to a fabrication error, each probe was made with only two of the four static pressure ports as designed. These holes were located on the port and starboard side of the probe tube, ten diameters downstream of the conical tip.

Table 3 Test (instrumentation) configurations and tunnel total pressures.

Configuration	Upstream	Rake plane x, inch	Downstream	Rake plane x, inch	p_{01} psia
3	blanks		port/centerline/starboard pitot rakes	26.149	50
5	blanks		blanks		70–139
6	blanks		centerline static rake	24.949	20–139
7	blanks		centerline static rake	26.149	20–139
8	blanks		centerline static rake	27.349	20–139
9	pitot rakes[a]	5.250	blanks		20–141[b]
10	blanks		port pitot rake	26.149	70–139
11	blanks		port/starboard pitot rakes	26.149	20–50
12	blanks		starboard pitot rake	26.149	70–139
13	blanks		centerline pitot rake	24.949	20–139
14	blanks		centerline pitot rake	26.149	20–139
15	blanks		centerline pitot rake	27.349	20–139

[a] Consisting of centerline and two port offsets.

[b] Finer pressure sweep (for boundary-layer characterization) using increments of 5 psia.

used 150 psig CA. Sweeps across the full pressure range utilized both combustion air services. All conditions were tested with the Mach 3.5 nozzle block. Compression plate angle was always swept in the increasing direction and included 4.0, 5.0, 5.5, 6.0, 6.5, 7.0, 7.5, 8.0 degrees for data runs, except for configurations 3 and 11 which experienced blockage complications.

V. Results and Discussion

A. Test Section Blockage

As discussed in the introduction, wind tunnel blockage was a concern for this method since the sidewall compression hardware reduced the cross-sectional area available to the flow in the test section. Like previous work [4], this study defined blockage fraction as the projected cross-sectional area of the obstruction divided by the total cross-sectional area of the test section. Table 4 lists the geometric blockage fractions imposed by the CP hardware as a function of plate angle. Note the approximately linear relationship to α for these small angles. The blockage ranged from 16.7 % to 36.8 % and represented the minimum for the method (CPs only) since the installation of rakes (or a model) would add to the blockage seen by the wind tunnel. Figure 15 shows silhouettes of the CP hardware and three downstream rakes (i.e., the maximum blockage tested) as originally configured for starting the test section core flow (left, $\alpha = 2.0°$) and the CP backside flow between the plates and sidewalls (right, $\alpha = 8.0°$). Observe that the starting procedure for the CP backsides (which involved raising the plates to 8.0°) actually increased the apparent blockage for the core flow. The figure also tabulates the respective blockage fractions and shows the notional capture (2.400 by 4.033 inches) of the high-q flow. The transverse offset in the notional capture was due to model integration considerations [3]. The 2.0° setting was chosen for wind tunnel starting because it corresponded to a relatively minimal blockage (see Table 4) and loaded the plates from the front surface (as designed). The 8.0° setting was chosen for CP backside starting because it increased the divergence between the plate and sidewall to encourage the "swallowing" of shock structures at the leading edge. According to quasi-one-dimensional inviscid flow theory [4, 16], at $M_1 = 3.44$, the Kantrowitz limit for supersonic starting[‖] was 30.6 % and the isentropic limit for remaining started was 84.4 %.

Although the tunnel started with three rakes installed (30.2 % blockage—each rake contributed 4.5 %), it began to unstart as the compression plates were brought to 8.0° (50.3 % blockage) to start the flow behind them. Signs of unstart included upstream propagation of pressure disturbances (indicated by the fast-response sensors) and flutter/shaking of

---

[‖] Figure 17 of the 1x1 SWT user manual [14] suggested ≤ 26–27 % for starting inlet models at $M_1 = 3.44$; however, these recommendations are often conservative and highly specific to the hardware geometry [4].

Table 4 Geometric blockage fraction for compression plate hardware (no rakes).

α, deg	2.0	3.0	4.0	5.0	5.5	6.0	6.5	7.0	7.5	8.0
Blockage fraction, %	16.7	20.1	23.4	26.8	28.5	30.1	31.8	33.5	35.1	36.8

the plates (observed by cameras looking through the ceiling windows). Even though the initial blockage fraction was marginally below the Kantrowitz limit (which becomes conservative at higher Mach numbers [4, 16, 17]), the final blockage fraction was considerably below the isentropic limit, and the blockage itself was axially distributed along the test section (which should relax the limits compared to consolidated blockage), the addition of aerodynamic blockage (due to only partial starting between the rakes and behind the plates) exceeded the tunnel's capacity for remaining fully started. Accordingly, the test was stopped and the centerline rake was removed, leaving the port and starboard rakes installed. Even with only these rakes installed, the compression plates again showed signs of unstarting for $\alpha \geq 7.5°$ (≥ 44.1 % blockage): aerodynamic flutter of the plates and growing unsteadiness in the ostensibly steady-state data.[**] Therefore, only data up to 7.0° are presented for that pressure sweep (in Fig. 25), and the remaining testing utilized a single rake (reducing blockage to 21.2–41.3 % for 2.0–8.0°) to afford the best results, free of any blockage-induced effects.

B. Starting of Wind Tunnel and Compression Plate Backsides

The compression plates are located as close as possible to the sidewalls to maximize the size of the test kite. However, this proximity to the sidewalls effectively constricts the flow behind the plates, acting like localized blockage. Moreover, the flow in this region primarily consists of low-momentum fluid from the boundary layer. Thus, concerns arise about the difficulty of starting the compression plates. To alleviate these concerns, a simple and reliable operational procedure was developed.

With the compression plates held at 2.0° and the diffuser initially equal to altitude exhaust pressure (approximately 1.8 psia), the tunnel core flow started at p_{01} = 35–40 psia as the plenum was slowly ramped to maximum operating pressure (approximately 50 or 140 psia, depending on the combustion air source). Once the tunnel supersonically started, the compression plates were swept up to 8.0° to fully start their backside. Figure 16 shows that the backside of the plates started at 6.5° for the port side and 6.0° for the starboard side. The plates were then returned to 3.8° prior to going to 4.0° to always approach the sweep angles from the same direction (i.e., increasing α) for consistent data acquisition.

For both the ceiling and floor pressures shown in Fig. 17, the upstream pressures (< 25 inches) are on centerline whereas the downstream pressures (> 25 inches) are at port/starboard offsets (±3.000 inches off of centerline). The data shown in Fig. 17 are measured downstream of installed boundary-layer rakes (configuration 9), which may perturb the measurement compared to an empty tunnel (configuration 5). Figure 17 shows the suppression of the upstream propagation of disturbances (i.e., the hump between 10 and 15 inches dissipates) with increasing plate angle.

C. Upstream Boundary Layer

Figures 18 and 19 display the upstream (i.e., incoming) boundary-layer results as measured by the short, cantilever pitot rakes[††] shown in Fig. 11. In particular, Fig. 18 shows the transverse Mach profiles for two test conditions, the lowest and highest total pressure (Reynolds number[‡‡]), at three spanwise locations. As expected from prior tunnel surveys [5], the Mach (velocity) deficit grows in height as the measurement location approaches the centerline (i.e., the center of the bulge). Furthermore, of the two conditions shown, the higher pressure one (plotted in red) has a slightly fuller profile (closer to the inviscid value) because of its greater Reynolds number. Also, the freestream Mach numbers agree with the nominal effective value of M_1 = 3.44 (dashed line). These Mach profiles (along with ones not shown) and the appropriate compressible formulas [13] yield the 99-percent (triangles, δ), displacement (asterisks, δ^*) and momentum (circles, θ) thicknesses for Fig. 19. As in the previous figure, left-to-right comparison of the subfigures readily conveys the boundary-layer growth in the spanwise direction toward the center of the tunnel. Although the boundary layer generally thins with increasing total pressure (or Reynolds number) as anticipated, over approximately

---

[**] The port/starboard pitot pressure profiles near the flow and ceiling of Fig. 25 contrast with those of Fig. 26 not only because of Reynolds number effects, but also blockage effects, since the former data were acquired by two simultaneous rakes instead of one rake at a time.

[††] The rake base static taps were located far enough aft to be influenced by the rake bodies; therefore, they were replaced with unperturbed readings from the ceiling centerline static tap at x = 5.200 inch.

[‡‡] Refer to Fig. 9 for the correspondence between Re_1 and p_{01}.

40–60 psia, the boundary layer experiences an unexpected thickening that becomes more pronounced towards the centerline. Since this pressure range overlaps with the changeover in combustion air service at 50 psia, one might attribute the thickening to that. However, closer inspection reveals that this trend slightly precedes the changeover point, eliminating this possibility. Moreover, the two CA services exhibit no noteworthy differences in steadiness or freestream conditions (Fig. 9). The authors hypothesize that movement of the counter-rotating vortex pair (responsible for the existence of the boundary-layer bulge) causes this thickening over 40–60 psia since streamwise development of the bulge can be non-monotonic and depends on the location of the vortices [6]. Nevertheless, this unexpected and as-yet-unexplained observation warrants further study.

Lastly, the compression plates were designed [3] to have enough clearance between their backside and the sidewall to permit supersonic flow and prevent their leading edge from immersing into the sidewall boundary layer (i.e., $d > \delta$). Comparing the thinner portion of the floor boundary layer (Port Offset 1 and 2 in Fig. 19) to the values of d in Table 5, one finds $d > \delta$, as desired. However, Fig. 4(b) indicates this region of the floor boundary layer is actually thinner than the sidewall boundary layer, so additional measurements should be made to confirm that the leading edge indeed remains in the freestream.

Table 5 Spanwise distance of leading edge from sidewall for compression plate angles.

α, deg	2.0	3.0	4.0	5.0	5.5	6.0	6.5	7.0	7.5	8.0
d, inch	1.537	1.489	1.441	1.393	1.369	1.345	1.321	1.296	1.272	1.248
d/w, %	12.6	12.2	11.8	11.4	11.2	11.0	10.8	10.6	10.4	10.2

D. Surface Static Pressure Measurements

Figures 20 and 21 plot the axial distribution of static pressure on the floor and ceiling surfaces as a function of α (colors) and p_{01} (subfigure rows). The left and right subfigure columns respectively show measurements taken along the centerline and port/starboard offsets ($z = \pm 3.000$ inch). Pressure is normalized by p_{01}. Symmetry is indicated when like-colored traces lie on top of each other. The centerline pressures exhibit very good floor-to-ceiling symmetry over the tested conditions. The port/starboard offset pressures have moderately good axial symmetry at lower α and higher p_{01}; however, symmetry degrades for $\alpha \gtrsim 7.5°$ and decreasing p_{01}. The offset taps are located directly downstream of the compression plates (especially for $\alpha \geq 7.0°$) and thereby under the influence of the trailing edge expansion fan, the refracted shock and likely shockwave reflections off the sidewall. These flow structures probably interact with the boundary layer, explaining the dependence on total pressure (i.e., Reynolds number) in addition to plate angle.

For certain conditions, some of the port/starboard pressures demonstrate greater unsteadiness (i.e., larger error bars) than the centerline measurements. In particular, for $\alpha = 7.5°$, the starboard side displays notable unsteadiness for $p_{01} \geq 90$ psia which extends to the port side for $p_{01} \geq 115$ psia. For $\alpha = 8.0°$, the starboard side shows unsteadiness at $p_{01} = 139$ psia.

Lastly, the centerline floor and ceiling pressure traces reveal that the near-surface upstream influence of the flow compression begins considerably ahead ($x \approx 15.2$ inch) of the inviscid predictions (broken lines, $x \approx 20.9$–22.5 inch) with downstream peak pressures generally below expectations. These results agree with past observations [5] for a similar experimental setup in the 1x1 SWT. Also, a flow expansion occurs around $x \approx 28.2$ inch for $\alpha = 5.5°$ which moves upstream[§§] and strengthens as α increases. The presence of this effect illustrates the need for intake fences in Zone 3 to capture the high-q flow and isolate it from the effects of the trailing edge expansion.

E. Downstream Region (High-q Test Kite)

This section details the high-q core flow results, obtained from the downstream rake measurements. Except as otherwise noted, the figures plot transverse profiles of pressure or Mach number as a function of α (colors), axial station or x (subfigure columns), and p_{01} (subfigure rows). Predictions (broken lines) based on basic inviscid theory are superimposed. Pressure quantities are normalized by p_{01}, except for dynamic pressure which is normalized by q_1. The nominal values for these parameters are listed on the plots. Transverse height, y', is normalized by the test section height, $h = 12.0$ inch, such that $y'/h = 0$ and $y'/h = 1$ respectively correspond to the floor and ceiling. Markers and error bars respectively denote the mean and standard deviation of the 12 measurements acquired by the steady-state data

---

[§§] The whole test kite moves upstream for increasing α, see Figs. 10(a) through 10(c).

system at each condition. Line connectors are merely for plotting clarity and do not indicate measured or interpolated data in between markers.

Figures 22–24 show direct measurements of the centerline pitot pressure. As expected, increasing the compression plate angle raises the pitot pressure. The relative depression of pressures in the inner core (between roughly $y'/h \approx 0.4$–0.6) diminishes with travel downstream and the overall profile becomes more pointed in shape. Increasing α also produces a similar effect. Error bars (which indicate gross unsteadiness) are generally smaller in size than the markers. Immersion in the floor boundary layer depresses the pitot pressures notably at $y'/h = 0.136$ and moderately at $y'/h = 0.178$. The probes at these locations are closer to the floor than the uppermost probe ($y'/h = 0.803$) is to the ceiling, causing the asymmetry. This boundary-layer effect near the floor also appears in subsequent plots of centerline dynamic/total pressure and Mach number. Moreover, increasing p_{01} seems to have little impact on the profiles other than to suppress the influence of the floor's boundary layer. Apart from the measurements inside the boundary layer, the pitot pressures agree to within roughly 5 % (in normalized units) of the inviscid predictions.

Figures 25 and 26 indicate the spanwise extent of the test kite at $x = 26.149$ inch by plotting the port (circles) and starboard (triangles) pitot pressures against the centerline data (boxes) previously shown. Note the alternative subfigure layout in which p_{01} increases left-to-right, top-to-bottom, while axial station remains fixed. The port and starboard direct measurements are generally within several percent (in normalized units) of the centerline values in the middle of the core flow. Graphically, like-colored traces lie or nearly lie on top of each other, especially toward the floor and ceiling for the port and starboard measurements. This result implies not only good side-to-side symmetry at this axial station, but that the high-q region spans the entire notional capture width (2.400 inches, shown in Figs. 1 and 15). Like the centerline plots, a region of depressed pitot pressures is found near the inner core which recovers as plate angle increases. Furthermore, the floor boundary layer affects the port and starboard measurements at $y'/h = 0.136$ and $y'/h = 0.178$ dramatically less than the centerline measurements (which literally fall off the chart). Since these two rakes are offset from centerline by ± 1.200 inch, some indication is given of the spanwise extent of the floor's boundary-layer bulge at $x = 26.149$ inch. Of course, increasing p_{01} reduces the height and influence of the floor boundary layer. Lastly, recall that the lower pressure measurements (20–50 psia, Fig. 25) used two simultaneous rakes and therefore suffered from the confounding effect of blockage, especially at the higher plate angles. Evidence of this effect includes the odd profile curvature near the floor and ceiling seen in Fig. 25 and the significant unsteadiness for $\alpha \geq 7.5°$ which has been omitted from Fig. 25 for clarity.

Figures 27–29 show direct measurements of the centerline static pressure. The core flow measurements were obtained from the static rake while the floor and ceiling measurements were interpolated/extrapolated from data acquired by the rake blank static taps in a separate run (configuration 5). As desired, sidewall flowfield compression raises the static pressure above its incoming value of $p_1/p_{01} \approx 1.4$ % shown in Figs. 20 and 21. Increasing α yields greater compression overall (higher static pressures), but also changes the profile shape, sometimes leading to a jagged profile. This transverse variation exceeds the minimum ESP transducer resolution of < 0.04 % (in normalized units), but may lie within the margin of error for the static pressure measurements as a whole. At higher p_{01}, the inner core flow experiences relatively stronger compression, giving rise to a more pointed shape, especially farther downstream. Similarly, travel downstream exacerbates the jaggedness at lower p_{01} and higher α, but confines the highest pressure rise to the inner core at elevated p_{01}—observe the sharply pointed profiles for $p_{01} \gtrsim 50$ psia and $x = 27.349$ inch in Figs. 28 and 29. The pointed shape likely stems from the glancing/refracting SWBLIs along the floor and ceiling (see Sec. III.B and Figs. 6(b) and 7(b)), and warrants further study by higher fidelity CFD. Some of the noticeable profile asymmetry results from the lowermost probe being closer to floor than the uppermost probe to the ceiling. Increasing p_{01} suppresses the boundary layer and improves the top-to-bottom symmetry.

Pertaining to Figs. 27–29, the coarser spatial discretization of the static measurements was necessary to minimize the interference between probes on the static rake. The authors originally planned to interpolate the static pressures in between measurement points to achieve the same spatial resolution as the pitot pressures; however, the static pressure profiles proved to be more complicated and less amenable to interpolation—interpolation would lead to unrealistic calculated quantities for Zone 3. Therefore, interpolation was not employed and the static pressure profiles and resulting calculated quantities (M_3, q_3 and p_{03}) have relatively coarse spatial resolution in the transverse direction. Lastly, as discussed in Sec. IV.C.2, the static measurements may be subject to error associated with the conical probes having fewer pressure ports than designed.

The preceding static and pitot pressures enable calculation (via the normal shock and isentropic relations [12, 13]) of centerline flow quantities in Zone 3 such as Mach number, M_3, dynamic pressure, q_3, and total pressure, p_{03}. In addition to the transverse profiles shown in Figs. 30–38, basic uniformity (or flow quality) metrics are computed at the target settings, $\alpha = 6.0°$, $p_{01} = 139$ psia and $x = 26.149$ inch. These target settings respectively correspond to satisfactory flow compression (and appropriate Mach number in Zone 3) [3], fluid dynamic similarity to the 10x10 SWT operating in propulsion cycle [3], and the entrance plane of the high-q notional capture (Figs. 1 and 15). The metrics are based on only four points in the core flow ($y'/h = 0.303$–0.803) because of the limited spatial resolution of the static measurements and the neglect of the lowermost point ($y'/h = 0.136$) engulfed by the floor's boundary layer. Observe that these four points cover 6.000 inches or 50.0 % of the test section height and are assumed to characterize the central 2.400 inches[¶¶] or 19.7 % of the test section width at the plane of $x = 26.149$ inch. For any future work, higher fidelity static pressure measurements are recommended due to the limited spatial resolution (and perhaps accuracy) of the calculated quantities and flow quality metrics.

Figures 30–32 show the calculated profiles of centerline Mach number. As expected, M_3 decreases with increasing α. Furthermore, M_3 generally increases as p_{01} increases (perhaps due to suppression of the boundary layer which would otherwise tend to choke the supersonic flow). At the target condition ($\alpha = 6.0°$, $p_{01} = 139$ psia and $x = 26.149$ inch), the spatial mean and standard deviation are $M_3 \approx 2.85 \pm 0.04$, or about 3 % above the inviscid prediction.

Figures 33–35 show the calculated profiles of centerline dynamic pressure ratio, q_3/q_1. As expected, the overall dynamic pressure ratio increases for advancing compression plate angle. The inner core flow benefits the most from increasing α and travel downstream magnifies this effect. The peak ratios exceed the inviscid predictions. At the target condition ($\alpha = 6.0°$, $p_{01} = 139$ psia and $x = 26.149$ inch), the spatial mean and standard deviation are $q_3/q_1 \approx 1.73 \pm 0.08$, or about 2 % above the inviscid prediction.

Figures 36–38 show the calculated profiles of centerline total pressure. As anticipated, p_{03}/p_{01} decreases with increasing α due to the lower total pressure recovery associated with stronger oblique shockwaves. Also, p_{03}/p_{01} improves near the floor (not shown) and ceiling with increasing p_{01} because of the progressively thinner boundary layer. Observe that the calculated total pressures generally exceed the inviscid predictions and, in many cases, 100 % (i.e., $p_{03} > p_{01}$). Although values over 100 % are not physically realizable in the current setup, the calculated total pressures are nevertheless within roughly 5 % (in normalized units) of expectation. This error is mostly due to the sensitivity of these calculations to the static pressure measurements, which contain greater uncertainty than the pitot pressures. Furthermore, the sidewall compression method, by very nature, minimally degrades total pressure, so it is unremarkable to calculate values in excess of 100 % given a somewhat elevated margin of error. At the target condition ($\alpha = 6.0°$, $p_{01} = 139$ psia and $x = 26.149$ inch), the spatial mean and standard deviation are $p_{03}/p_{01} \approx 1.01 \pm 0.02$, or about 4 % above the inviscid prediction. In terms of a flow distortion metric, $\frac{\max(p_{03})-\min(p_{03})}{\mathrm{mean}(p_{03})} < 5\,\%$, implying minimal transverse distortion.

F. Steadiness of Pressure Data

A gross indication of steadiness is given by the error bars (standard deviations) in the preceding data figures. However, since the steady-state data system acquired these measurements, the standard deviations are based on relatively few samples (12 each) and relatively slow sampling rates (1 Hz). A better quantification of steadiness is given by the fast-response sensors embedded in the upstream and downstream centerline rake blanks on the test section floor. The dynamic data system operates these sensors at a frequency of 20 kHz and takes approximately 320 000 samples for each acquisition. Figure 39 shows the dynamic data results for the tunnel without rakes installed (i.e., blanks only or configuration 5) plotted in terms of the ratio of the standard deviation to the mean. The Zone 1 (triangles) and Zone 3 (boxes) sensors are located on centerline at $x = 5.750$ inch and $x = 26.700$ inch, respectively. The figure illustrates several trends. First, the standard deviation decreases with increasing tunnel total pressure (Reynolds number) for both zones, especially for the lowest pressures in Zone 1 (Zone 3 lacks data for $p_{01} \leq 50$ psia, but similar trends are anticipated). Second, Zone 1 shows an independence with plate angle, expected since it lies upstream of the plates in a supersonic flowfield. Third, the baseline value of unsteadiness for Zone 3 is higher than Zone 1 and progressively increases for $\alpha \geq 6.5°$. This third trend is likely explained by the shockwave/boundary-layer interaction at the shock crossing (upstream of the measurement location) contributing extra unsteadiness to the flow and the intensity of the SWBLI scaling with the oblique shock strength (i.e., compression plate angle).

Overall, the measured unsteadiness is small, less than several percent of the mean and comparable to (or even smaller than) the estimated accuracy of the sensor in absolute terms. Power spectral density plots (not shown) exhibit a broadband spectrum, with frequencies up to several kilohertz (the peak central frequency increases for $\alpha \gtrsim 6.5°$ in Zone 3). Although these results suggest only marginal unsteadiness, they are localized to the surface; therefore, follow-up work could be done to characterize the core flow in Zone 3 (for example, using a rake instrumented with fast-response sensors).

[¶¶] The centerline pitot pressures generally agree with the port and starboard offsets in Fig. 26, implying high-q flow between at least $z = \pm 1.200$ inch.

VI. Summary and Conclusions

A method for increasing the dynamic pressure in the test section of a supersonic wind tunnel is experimentally demonstrated. The method relies on symmetrically-opposed, variable-ramp-angle compression plates placed along the test section sidewalls to generate oblique shockwaves and thus produce a relatively uniform region of elevated dynamic pressure or high-q downstream of the shockwave refraction. This sidewall compression method is investigated from a theoretical, computational and experimental perspective, culminating in a reduced-scale, proof-of-concept test in the 1- by 1-Foot Supersonic Wind Tunnel at $M_1 = 3.44$ (Mach 3.5 nozzle block). The experiment utilizes upstream boundary-layer pitot rakes to sample the incoming flow conditions, downstream pitot and static rakes to measure the high-q core flow and numerous surface taps to map out the static pressure distribution.

A reliable and robust starting procedure is developed to establish supersonic flow in the tunnel and behind the compression plates. First, the tunnel is started with the plates at $\alpha = 2.0°$, and then the plate backside flow is started by raising the angle to 8.0°. Once started, the plate backsides remain started throughout the full range of test conditions ($\alpha = 4.0$–$8.0°$ and $p_{01} = 20$–139 psia). Of course, additional testing should be performed with representative model blockage in the test section and Mach numbers which mimic the 10x10 SWT starting procedure ($M = 2.0$–2.5).

The incoming boundary layer along the floor is characterized at three spanwise stations over the full operational range of the tunnel ($p_{01} = 20$–141 psia) for $M_1 = 3.44$. Previously documented features (such as the bulge in the boundary layer toward the centerline) are observed; however, an unexpected thickening of the boundary layer with increasing total pressure (i.e., Reynolds number) is discovered for $p_{01} \approx 40$–60 psia. The reason for this thickening is not presently known, but thought to originate in the movement of the counter-rotating vortex pair responsible for the existence of the bulge.

The high-q core flow is characterized for eight compression plate angles, eight tunnel total pressures (i.e., Reynolds numbers) and three axial stations. Centerline, port and starboard measurements at the entrance plane of the notional capture ($x = 26.149$ inch) confirm the presence of high-q flow at the conditions tested. Flow expansion farther downstream at higher plate angles affirms the need for intake fencing to properly capture the high-q stream and isolate it from the expansion fans which emanate off the compression plate trailing edges.

The centerline pitot and static pressure measurements facilitate calculation of Mach number, dynamic pressure and total pressure within the high-q region. The peak dynamic pressures ratios, q_3/q_1, exceed expectations. For the target conditions relevant to larger scale testing [3] ($\alpha = 6.0°$, $p_{01} = 139$ psia and $x = 26.149$ inch), the spatial mean and standard deviation are:

- $M_3 \approx 2.85 \pm 0.04$, or about 3 % above inviscid predictions
- $q_3/q_1 \approx 1.73 \pm 0.08$, or about 2 % above inviscid predictions
- $p_{03}/p_{01} \approx 1.01 \pm 0.02$, or about 4 % above inviscid predictions

In terms of flow distortion,

$$\frac{\max(p_{03}) - \min(p_{03})}{\mathrm{mean}(p_{03})} < 5\,\%,$$

implying acceptable distortion in the transverse direction. Although these metrics indicate good performance and uniformity, because of the limited spatial resolution of the static rake, they are based on four discrete points in the core flow—a relatively small number of points for statistics. Therefore, higher fidelity static measurements are needed to properly survey the region, confirm the trends and map out the full extent of the high-q test kite.

Limited dynamic data instrumentation suggests minimal unsteadiness in the upstream and downstream flow, less than a few percent of the mean and comparable to the estimated accuracy of the pressure sensor in absolute terms. Since these measurements were confined to the floor surface, additional measurements could be taken in the core flow, although the present dynamic data pose little reason to worry about unsteadiness in the core.

VII. Next Steps

The data collected thus far have provided great insight into the flow quality within the test kite region; however, a number of additional measurements and analyses are desired to complete the technique assessment, including:

1) Sidewall boundary-layer measurements to verify that the compression plate leading edges always remain in the freestream,
2) More fully resolved static pressure measurements within the test kite region, either through additional staggered rakes or with a translatable rake probe,

3) Additional pitot and static pressure measurements in the offset positions of the test kite region to better define its size in comparison to the theoretical inviscid envelope,[***]
4) Perform higher fidelity CFD to better understand the origins of the test kite flow distortion. This analysis could also lead to strategies to minimize distortion, such as bleeding the oblique glancing/refracting SWBLI on the test section floor and ceiling. Moreover, surface flow visualization,[†††] which would not require any additional hardware, would be useful in determining if CFD captured the extent of any separation accurately.

In regards to the last item, it was previously mentioned that the orientation of the compression plates with the glancing/refracting SWBLI coinciding with the non-contoured nozzle flow surfaces (floor and ceiling) was done specifically to mimic potential technique application to other wind tunnel facilities. The aforementioned vortex pairs that develop along these surfaces are likely influenced by the nozzle geometry (length and aspect ratio) as well as flow conditions (Mach and Reynolds number). The thickening of the boundary layer makes the flow more susceptible to separation in the SWBLI region and likely contributes to flow distortion in the test kite region. Thus, it is important to better understand how these vortex pairs develop based on flow conditions. Indeed, the results of this study indicate a Reynolds number dependence, as the boundary-layer thickness in the vortex region experiences a period of growth with Reynolds number which is contrary to the expected trend. Further, any experiment that is intended for CFD validation that does not isolate the flowfield of interest from the nozzle vortices will have to be able to capture them accurately. Thus, an experimental and numerical study of the origin and development of the nozzle vortices is also suggested.

Although the focus of this experiment was at a nominal freestream Mach number of 3.5 ($M_1 = 3.44$), there is potential interest in extending the study to other Mach numbers. In particular, for facilities that have flexible-wall nozzles that start at lower Mach numbers, there would be an interest in studying wind tunnel and compression plate backside startability at lower Mach numbers.

Finally, the compression plate hardware developed for this study is a significant capability enhancement for the 1x1 SWT. Although this capability was previously available, the hardware was not compatible with the new test section that was installed in the mid-1990s. The hardware can be configured to study a number of SWBLIs including oblique glancing, symmetric and asymmetric oblique glancing/refracting, and oblique impinging/reflecting. Further, the hardware can be rotated in the test section such that the compression plates span between the sidewalls.

References

[1] Fox, J. L., “Supersonic Tunnel Investigation by Means of Inclined-Plate Technique to Determine Performance of Several Nose Inlets over Mach Number Range of 1.72 to 2.18,” Tech. Rep. NACA RM E50K14, NACA Lewis Flight Propulsion Laboratory, Feb 1951.

[2] Hearth, D. P., Anderson, B. H., and Dryer, M., “Performance Comparison at Mach Numbers 1.8 and 2.0 of Full-Scale and Quarter-Scale Translating Spike Inlets,” Tech. Rep. NACA RM E57D16, NACA Lewis Flight Propulsion Laboratory, Oct 1957.

[3] Davis, D. O., “Development of a Test Configuration to Increase Dynamic Pressure in NASA GRC’s 1x1 Ft and 10x10 Ft Supersonic Wind Tunnels,” Tech. Rep. NASA/TM-20205010101, NASA Glenn Research Center, Dec 2020.

[4] Pastor-Barsi, C., Peters, C., and Vyas, M., “Summary of the 2017 Blockage Test in the 10- by 10-Foot Supersonic Wind Tunnel,” Tech. Rep. NASA/TM-2018-220016, NASA Glenn Research Center, Oct 2018.

[5] Davis, D. O., and Hingst, W. R., “Surface and Flow Field Measurements in a Symmetric Crossing Shock Wave/Turbulent Boundary-Layer Interaction,” Tech. Rep. NASA/TM-106086, NASA Lewis Research Center, June 1992.

[6] Mokhtari, S., and Bradshaw, P., “Longitudinal Vortices in Wind Tunnel Wall Boundary Layers,” *Aeronaut. J.*, Vol. 87, No. 866, 1983, pp. 233–236.

[7] Hearth, D. P., and Perchonok, E., “Performance of a 16-Inch Ram-Jet Engine with a Can-Type Combustor at Mach Numbers of 1.50 to 2.16,” Tech. Rep. NACA RM E54G13, NACA Lewis Flight Propulsion Laboratory, Aug 1954.

[8] Porcher, C. E., and Thebiay, F. J., “Development of the Variable Geometry Inlet for the B-58 Airplane,” *National Aerospace Engineering & Manufacturing Meeting*, Oct 1962.

[9] Hingst, W. R., and Williams, K. E., “Interaction of Two Glancing, Crossing Shock Waves with a Turbulent Boundary-Layer at Various Mach Numbers,” Tech. Rep. NASA/TM-103740, NASA Lewis Research Center, Sept 1991.

[***] Rakes capable of multi-axis traverse (e.g., along y and z) could accomplish these measurements at arbitrarily high spatial resolution.

[†††] For example, fluorescent oil flow visualization has been successfully used by similar experimental setups in the 1x1 SWT [5, 9, 10].

[10] Williams, K. E., and Hingst, W. R., “The Effect of Varying Mach Number on Crossing, Glancing Shocks / Turbulent Boundary-Layer Interactions,” *27th AIAA/SAE/ASME/ASEE Joint Propulsion Conference and Exhibit*, June 1991.

[11] Reddy, D. R., “3-D Navier-Stokes Analysis of Crossing, Glancing Shocks/Turbulent Boundary Layer Interactions,” *22nd AIAA Fluid Dynamics, Plasma Dynamics and Lasers Conference*, June 1991.

[12] Anderson, J. D., Jr., *Modern Compressible Flow with Historical Perspective*, 2nd ed., McGraw-Hill, Boston, 1990.

[13] Liepmann, H. W., and Roshko, A., *Elements of Gasdynamics*, 1st ed., Dover, Mineola, New York, 2001.

[14] Soeder, R. H., Stark, D. E., Leone, J. F.X., and Henry, M. W., “NASA Glenn 1- by 1-Foot Supersonic Wind Tunnel User Manual,” Tech. Rep. NASA/TM-1999-208478/REV1, NASA Glenn Research Center, Dec 2003.

[15] Soeder, R. H., Roeder, J. W., Linne, A. A., and Panek, J. W., “User Manual for NASA Glenn 10- by 10-Foot Supersonic Wind Tunnel,” Tech. Rep. NASA/TM-2004-212697, NASA Glenn Research Center, May 2004.

[16] Van Wie, D. M., Kwok, F. T., and Walsh, R. F., “Starting Characteristics of Supersonic Inlets,” *32nd AIAA/ASME/SAE/ASEE Joint Propulsion Conference and Exhibit*, July 1996.

[17] Draper, A. C., “Redefinition of the Limiting Concept for Supersonic Wind Tunnel Blockage,” Tech. Rep. AD-155-692, Wright Air Development Center, June 1958.

Figures

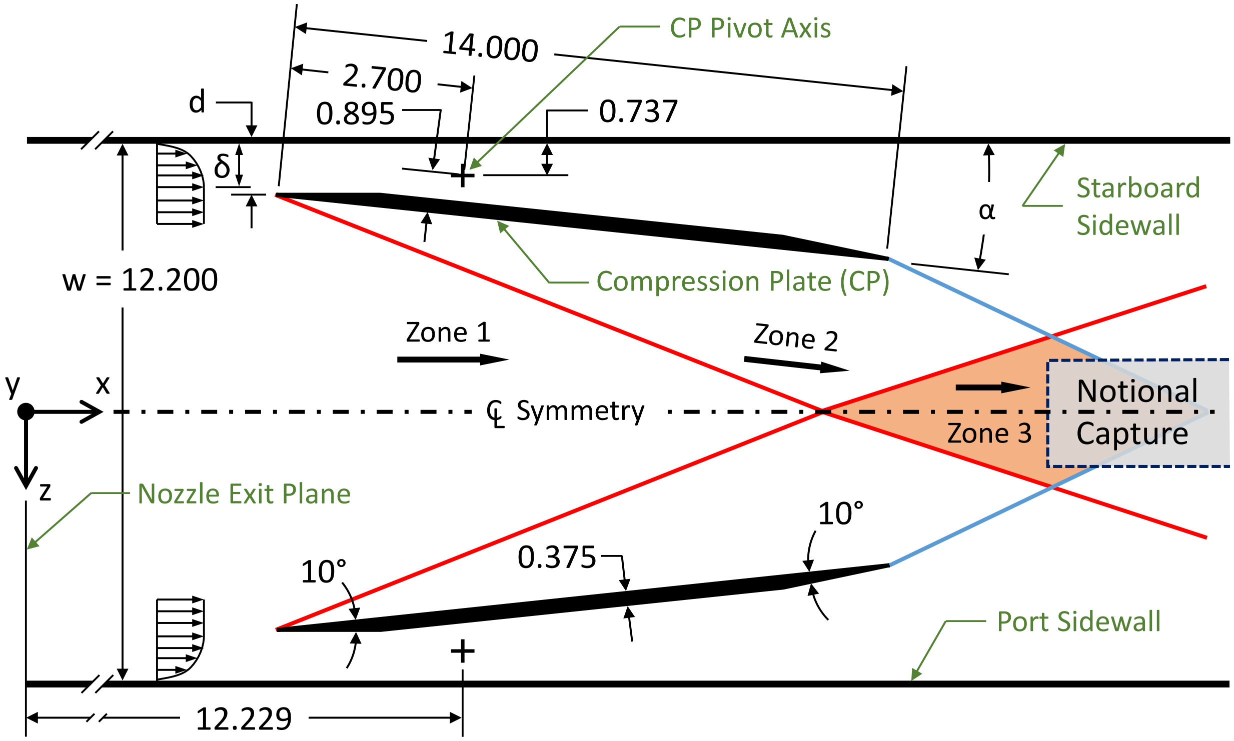

Fig. 1 Plan-view diagram of compression plate geometry in wind tunnel test section. Nominal length dimensions in inches. Assumes $d > \delta$, see Table 5 for values of d. Adapted from Davis [3].

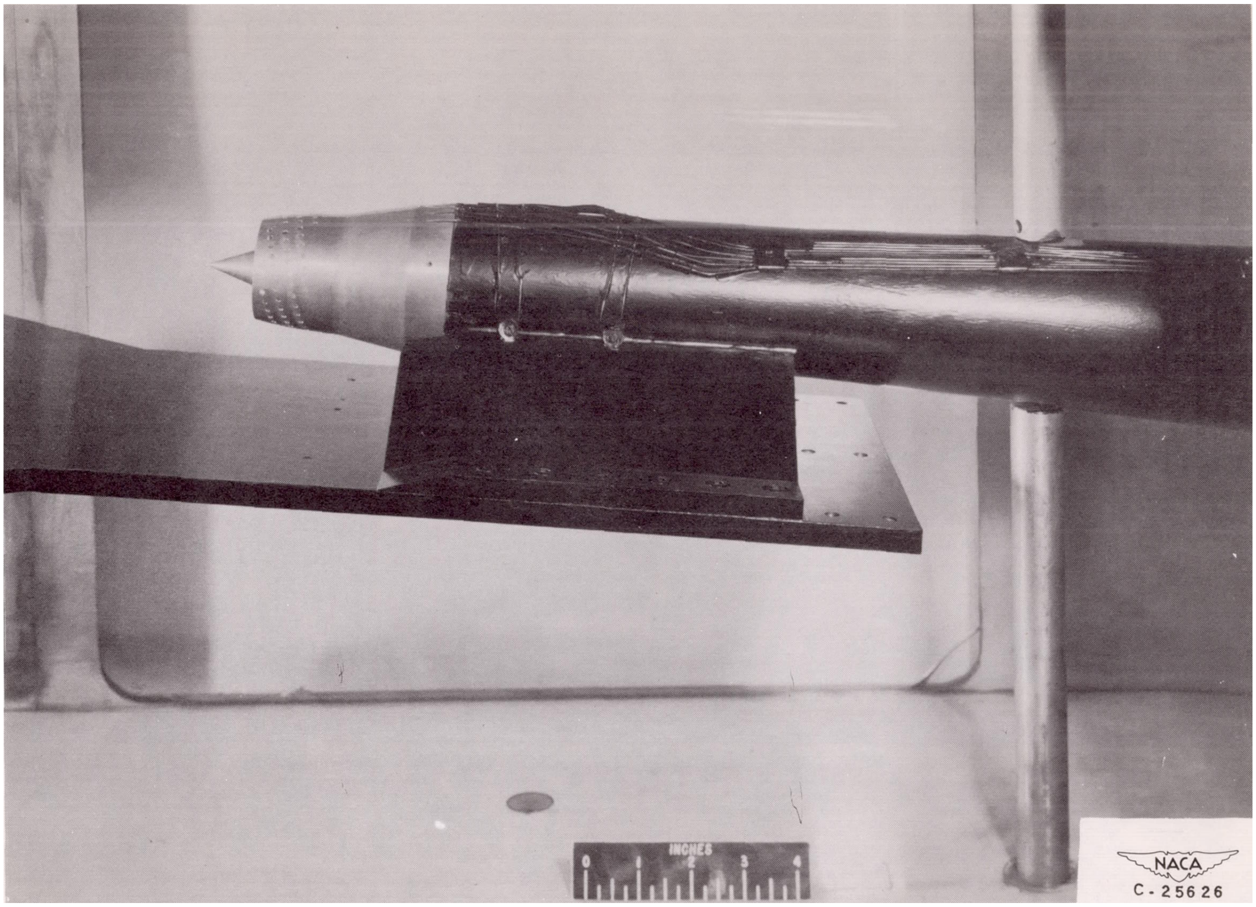

(a) For inlet testing in the former 18- by 18-Inch Supersonic Wind Tunnel [1].

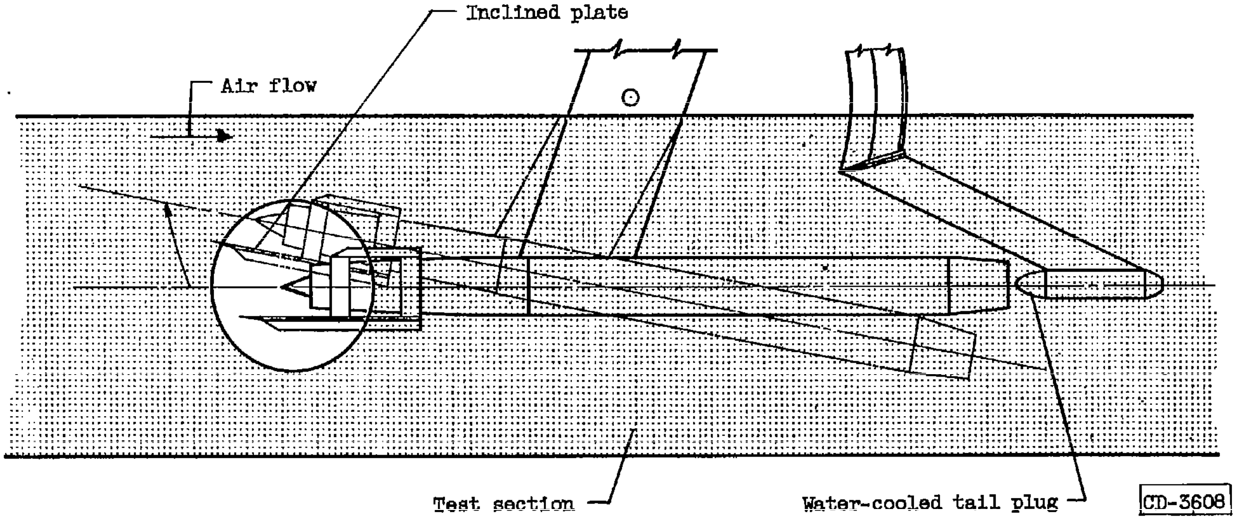

(b) For ramjet testing in the 8- by 6-Foot Supersonic Wind Tunnel [7].

Fig. 2 Model-mounted compression/expansion plates.

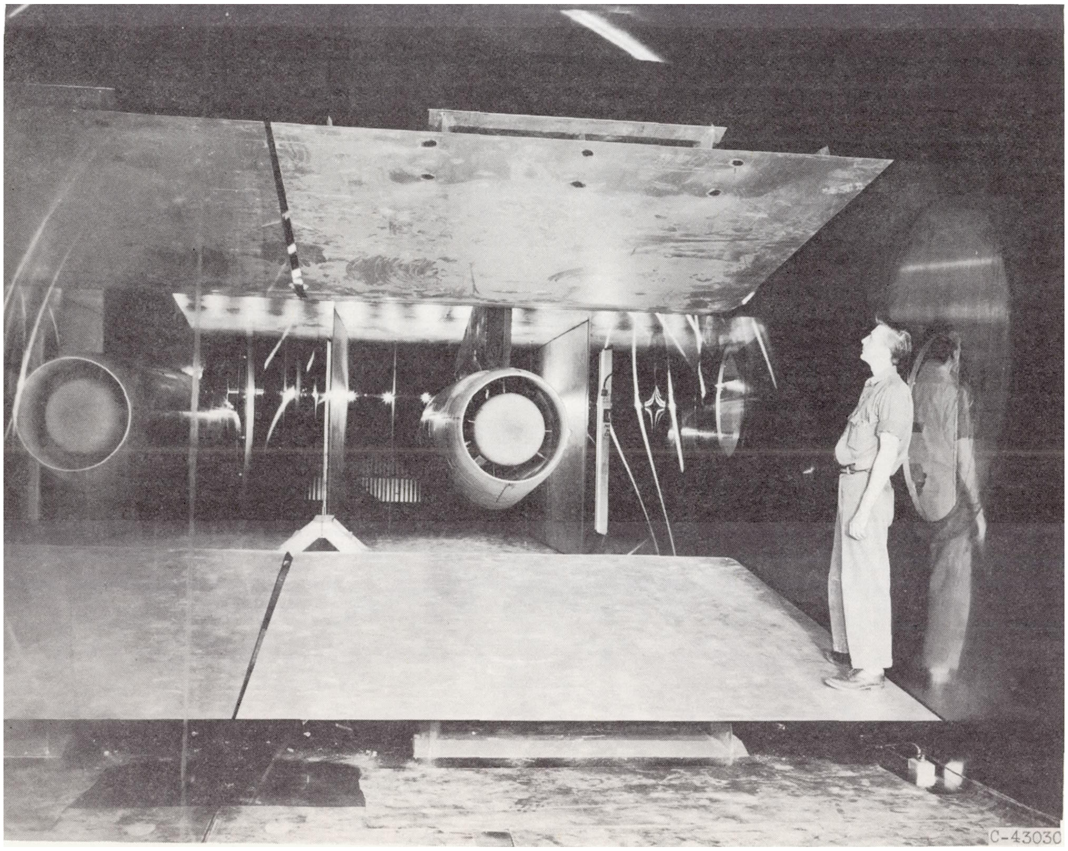

(a) Compression plates installed on the floor and ceiling of the 10x10 SWT [2].

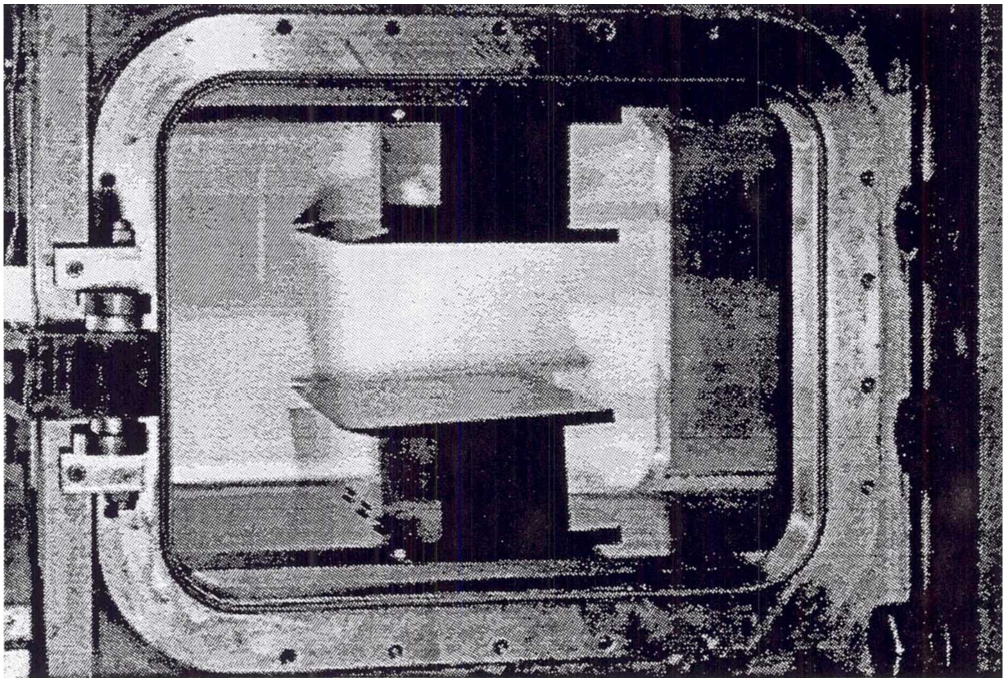

(b) Compression plates in the 1x1 SWT [9].

Fig. 3 Facility-mounted compression plates.

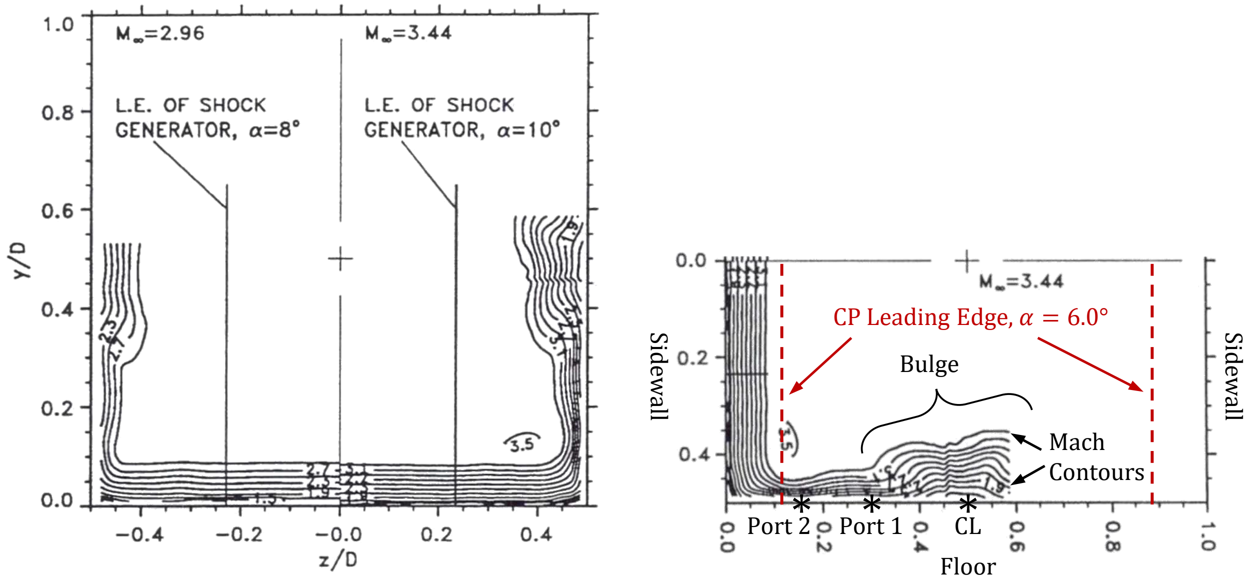

(a) Sidewall boundary-layer interaction [5].

(b) Floor/ceiling boundary-layer interaction. Asterisks demarcate upstream rake locations in present experiment. Adapted from Ref. [5].

Fig. 4 Boundary-layer interactions.

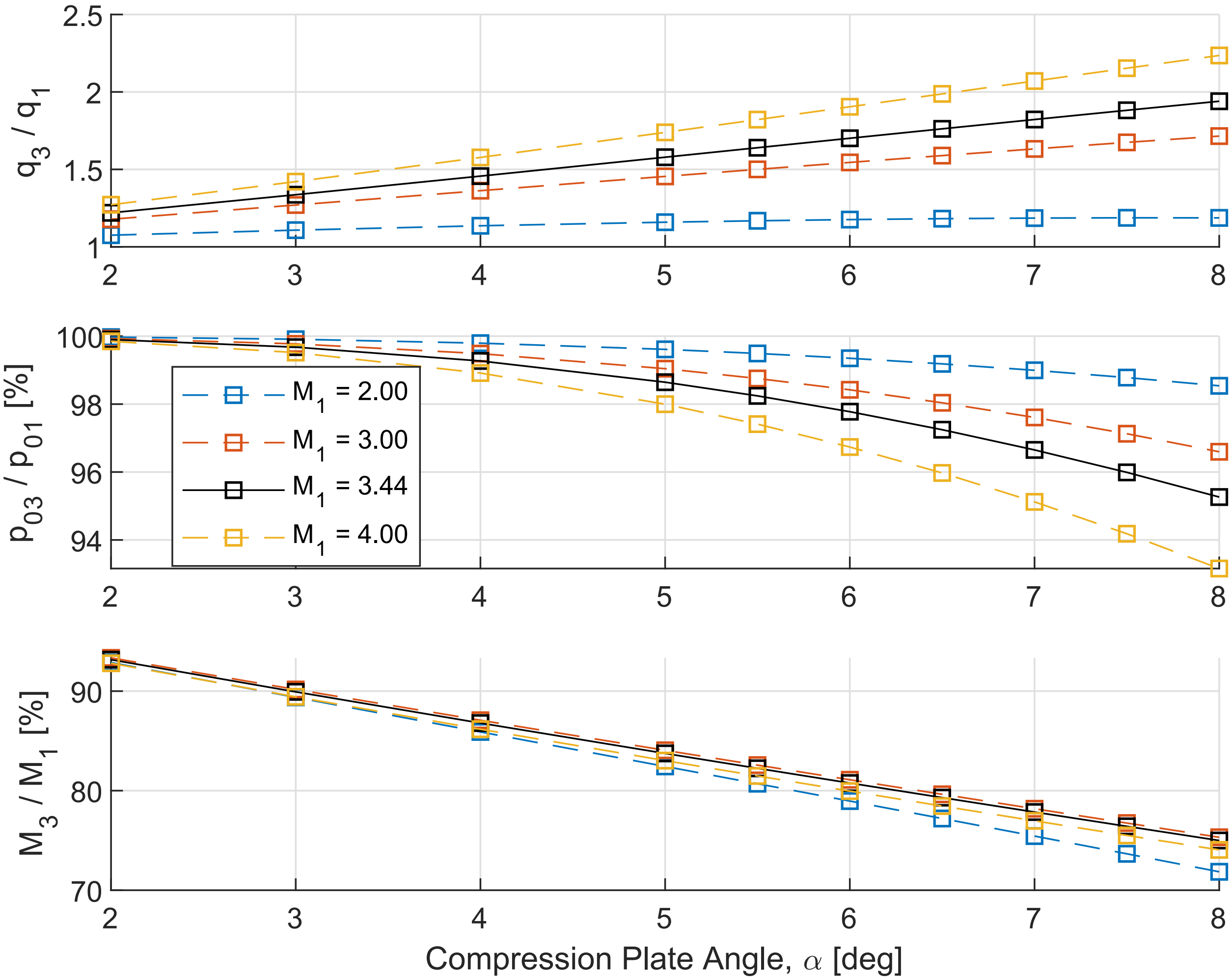

Fig. 5 Theoretical performance (ratios of Zone 3 to Zone 1 quantities) as function of plate angle for sidewall compression method. M_1 = 3.44 results (black lines) apply to present study.

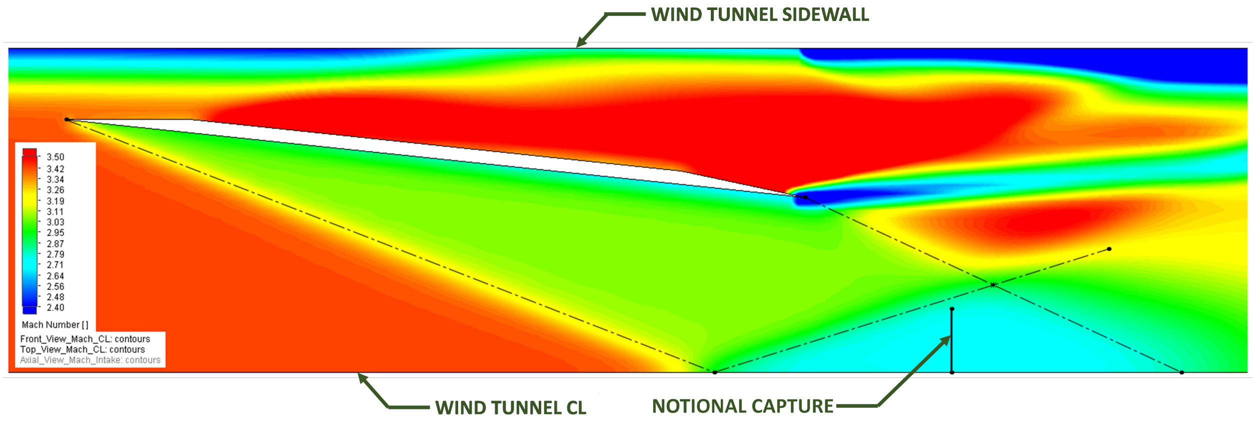

(a) Centerline cut, plan view.

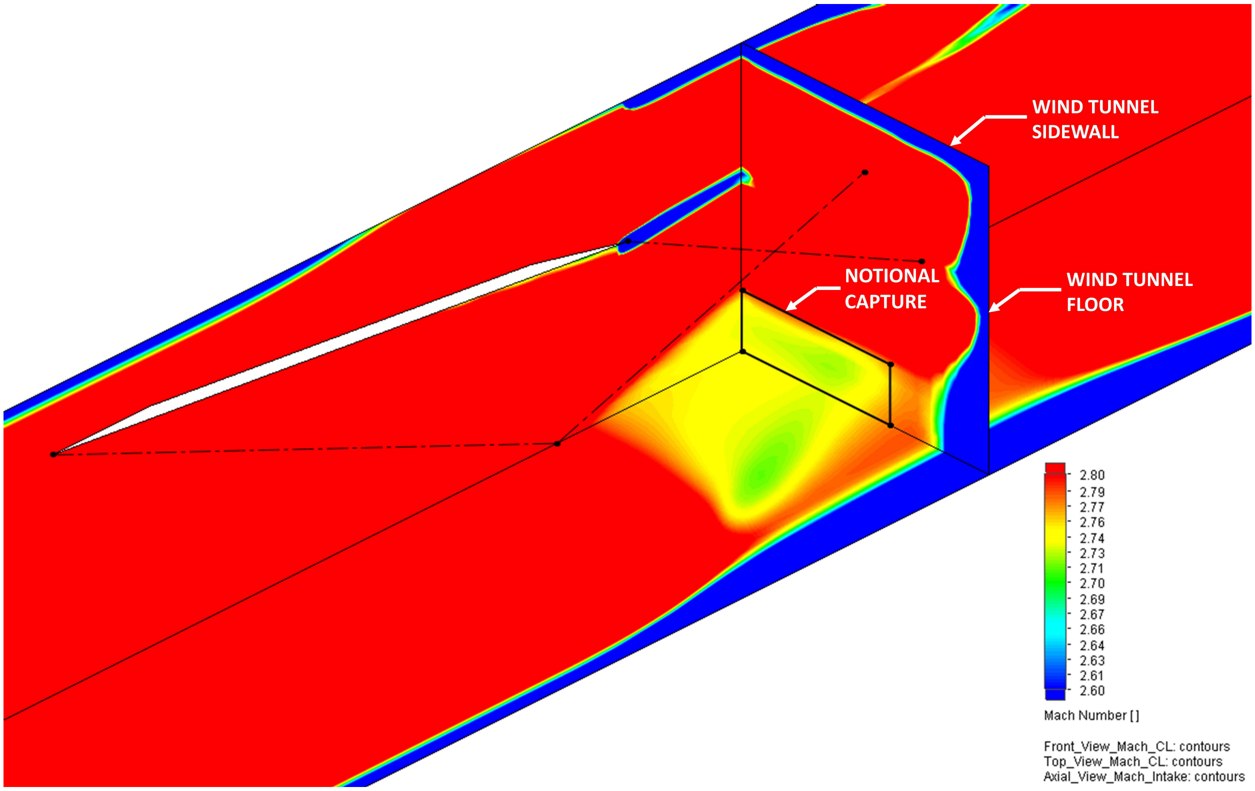

(b) Centerline and notional capture plane cuts, isometric view.

Fig. 6 Results for $M_1 = 3.44$, $Re_1 = 16.8 \times 10^6$ (width basis) and $\alpha = 6.0°$ [3]. Note that upper and lower figures use different scaling for clarity.

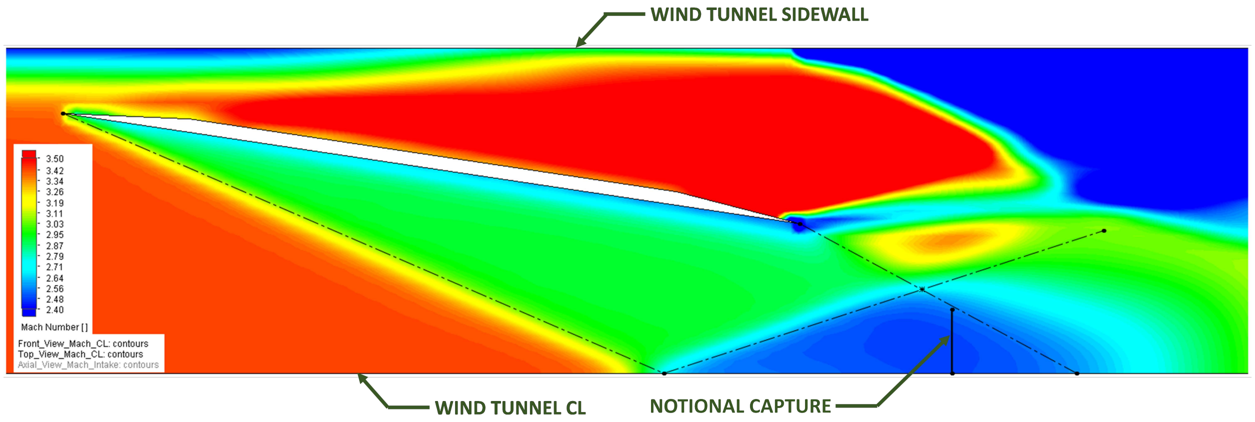

(a) Centerline cut, plan view.

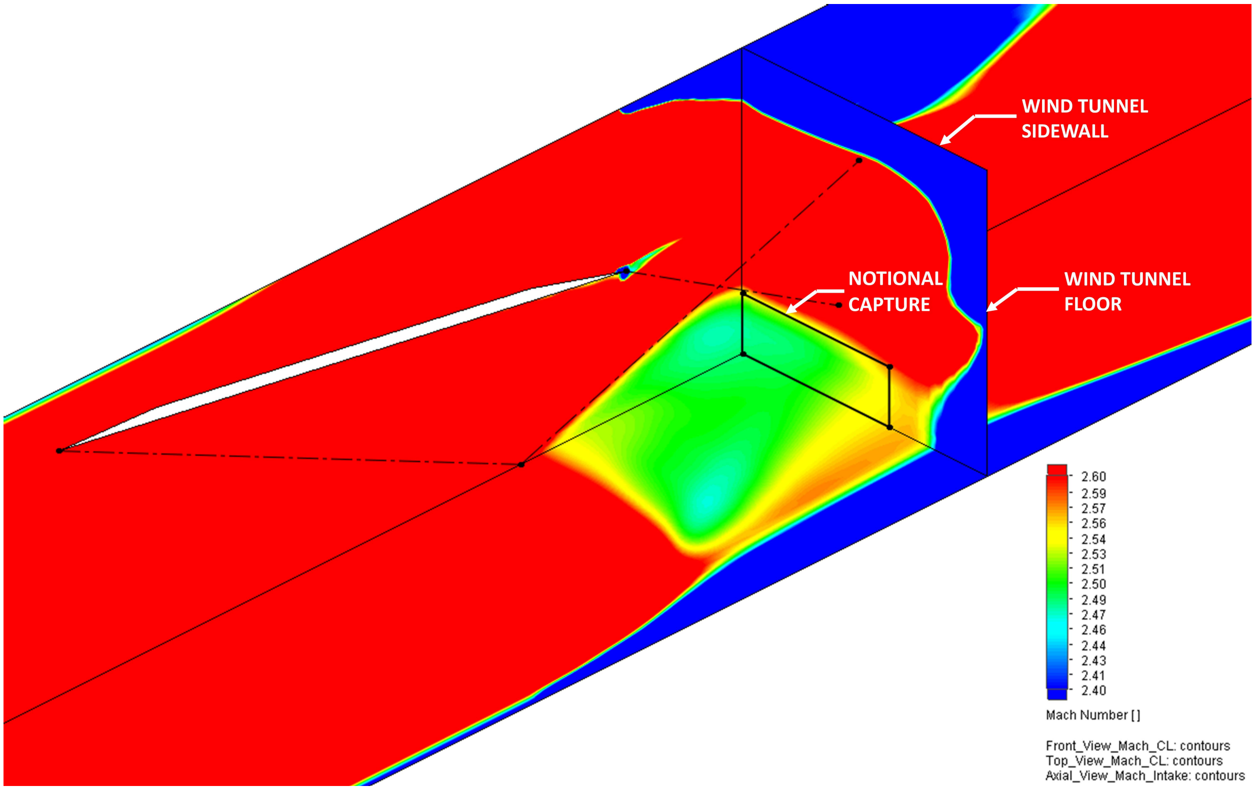

(b) Centerline and notional capture plane cuts, isometric view.

Fig. 7 Results for $M_1 = 3.44$, $Re_1 = 16.8 \times 10^6$ (width basis) and $\alpha = 8.5°$ [3]. Note that upper and lower figures use different scaling for clarity.

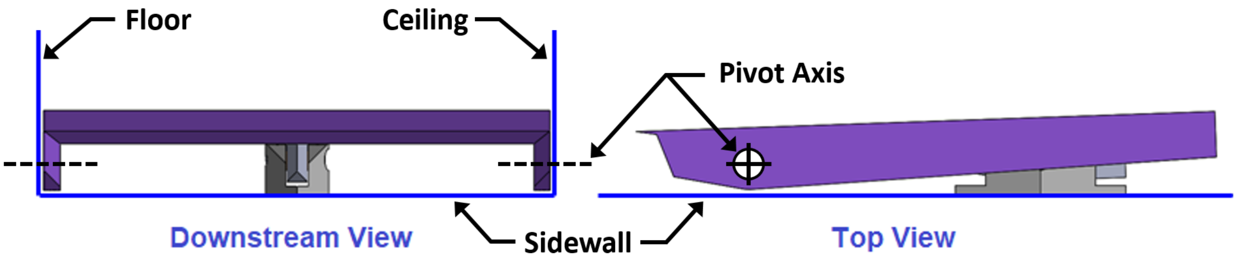

(a) Compression plate hardware with pivot design details.

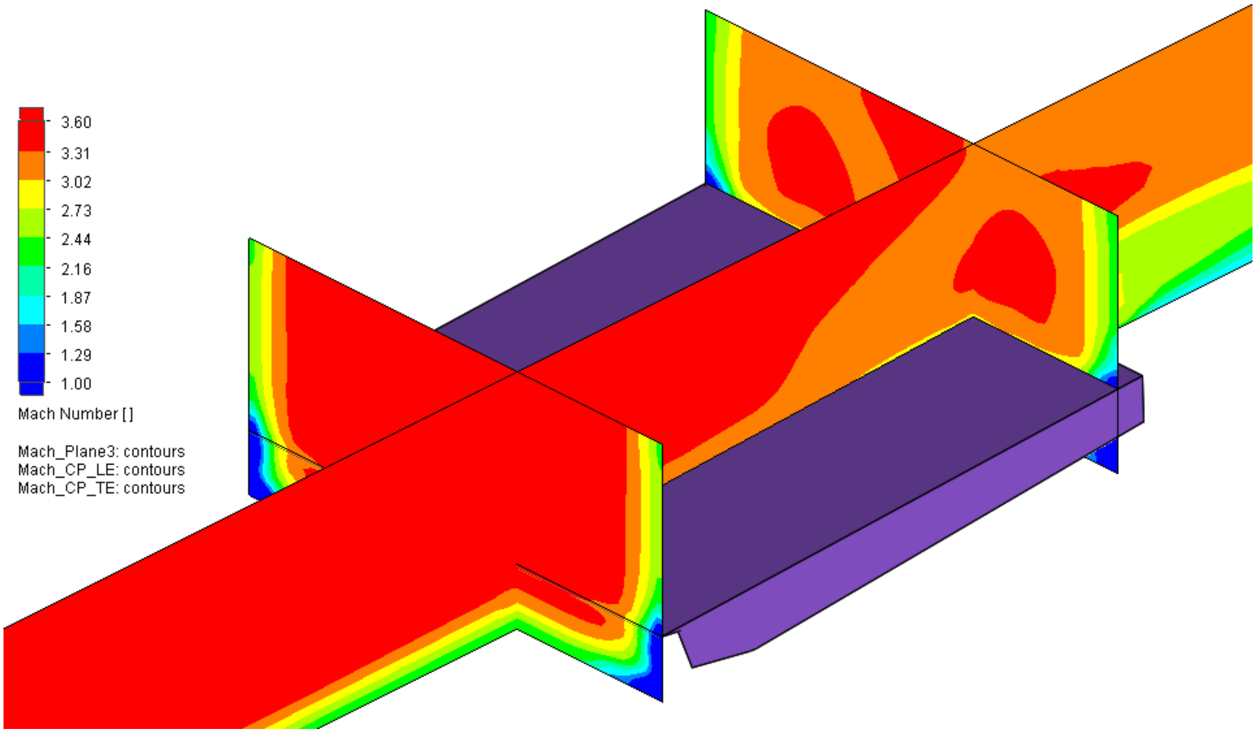

(b) Mach contours around CP for $M_1 = 3.44$, $Re_1 = 16.8 \times 10^6$ (width basis) and $\alpha = 2.0°$.

Fig. 8 Compression plate hardware with improved pivot design [3].

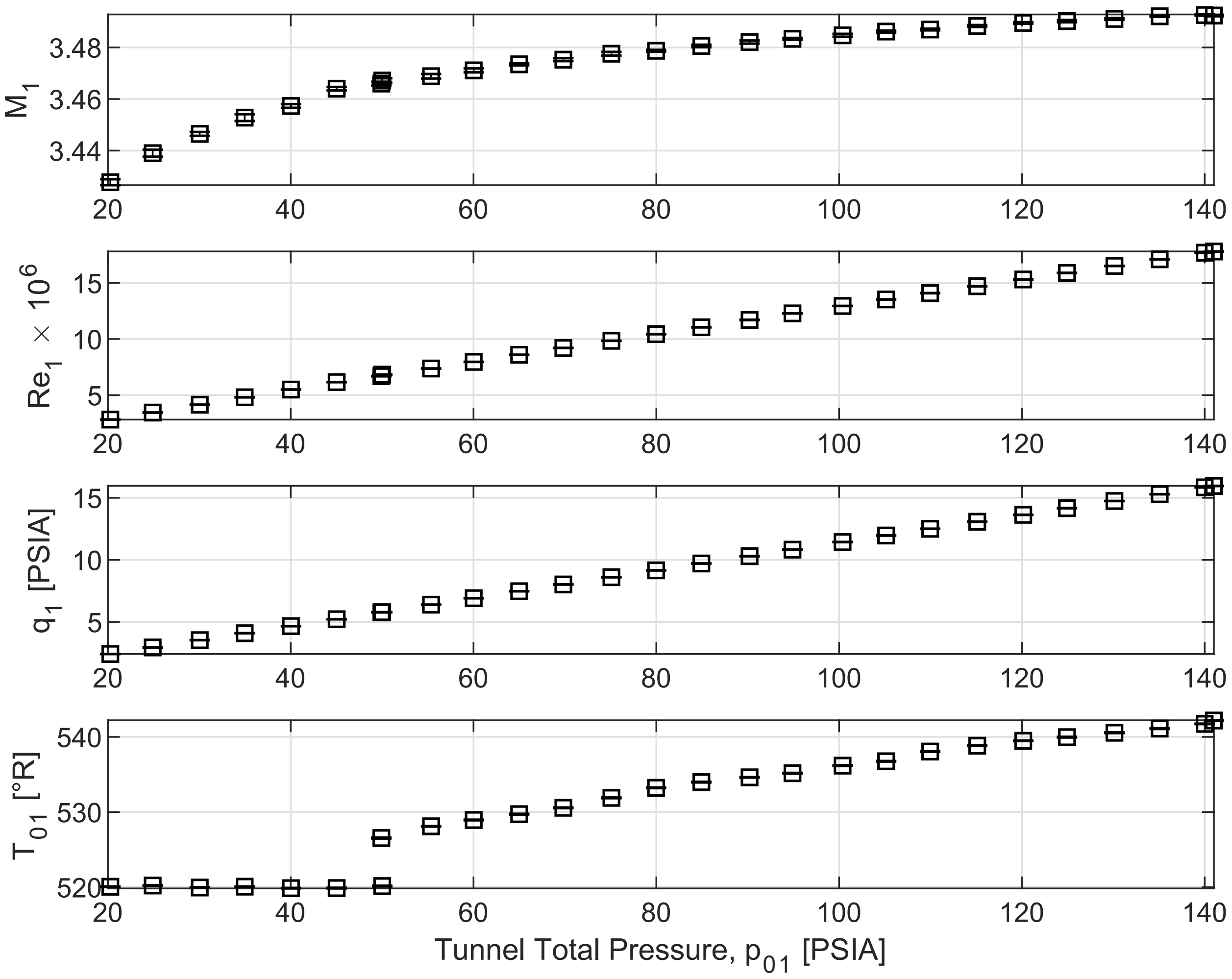

Fig. 9 Representative values of tunnel (i.e., incoming) Mach number, Reynolds number (width basis), dynamic pressure and total temperature for tunnel total pressure setting.

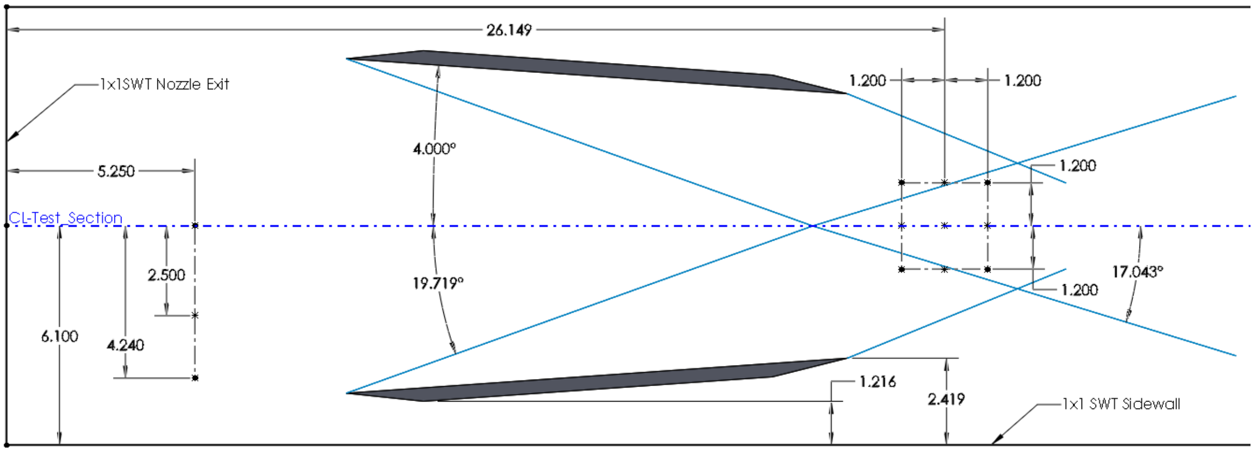

(a) Test kite for α = 4.0°.

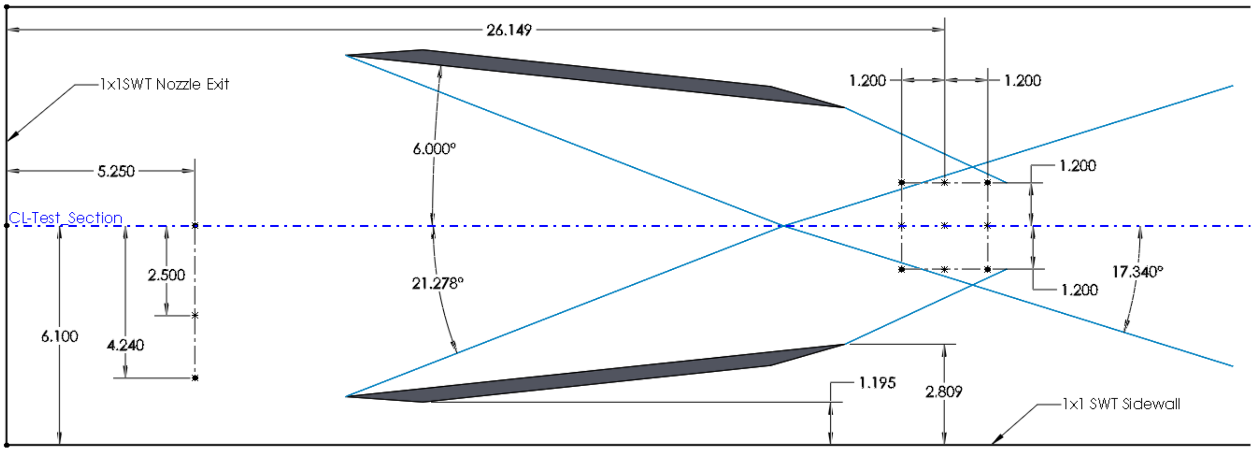

(b) Test kite for α = 6.0°.

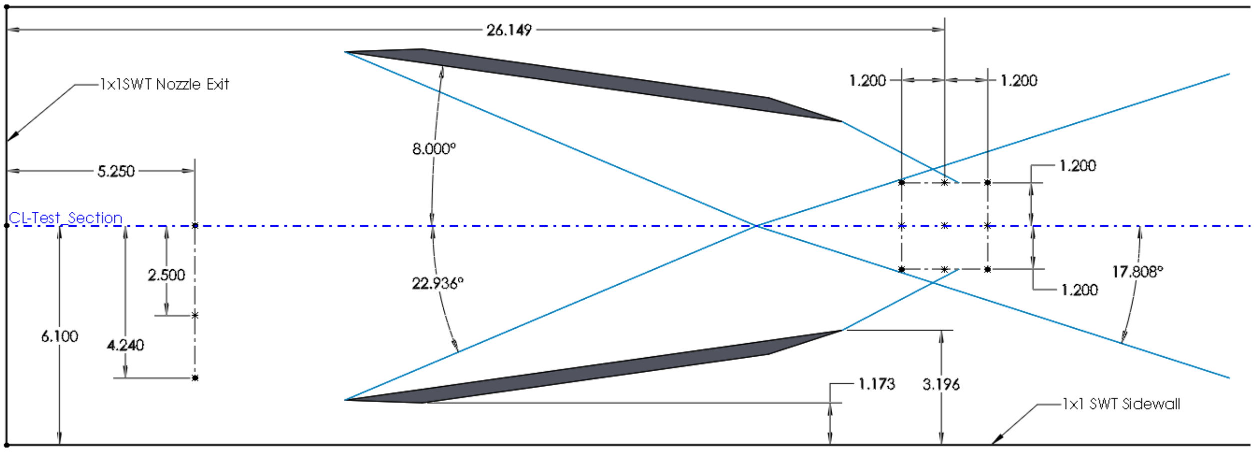

(c) Test kite for α = 8.0°.

Fig. 10 Test kite evolution with respect to the three upstream and nine downstream rake locations (asterisks).

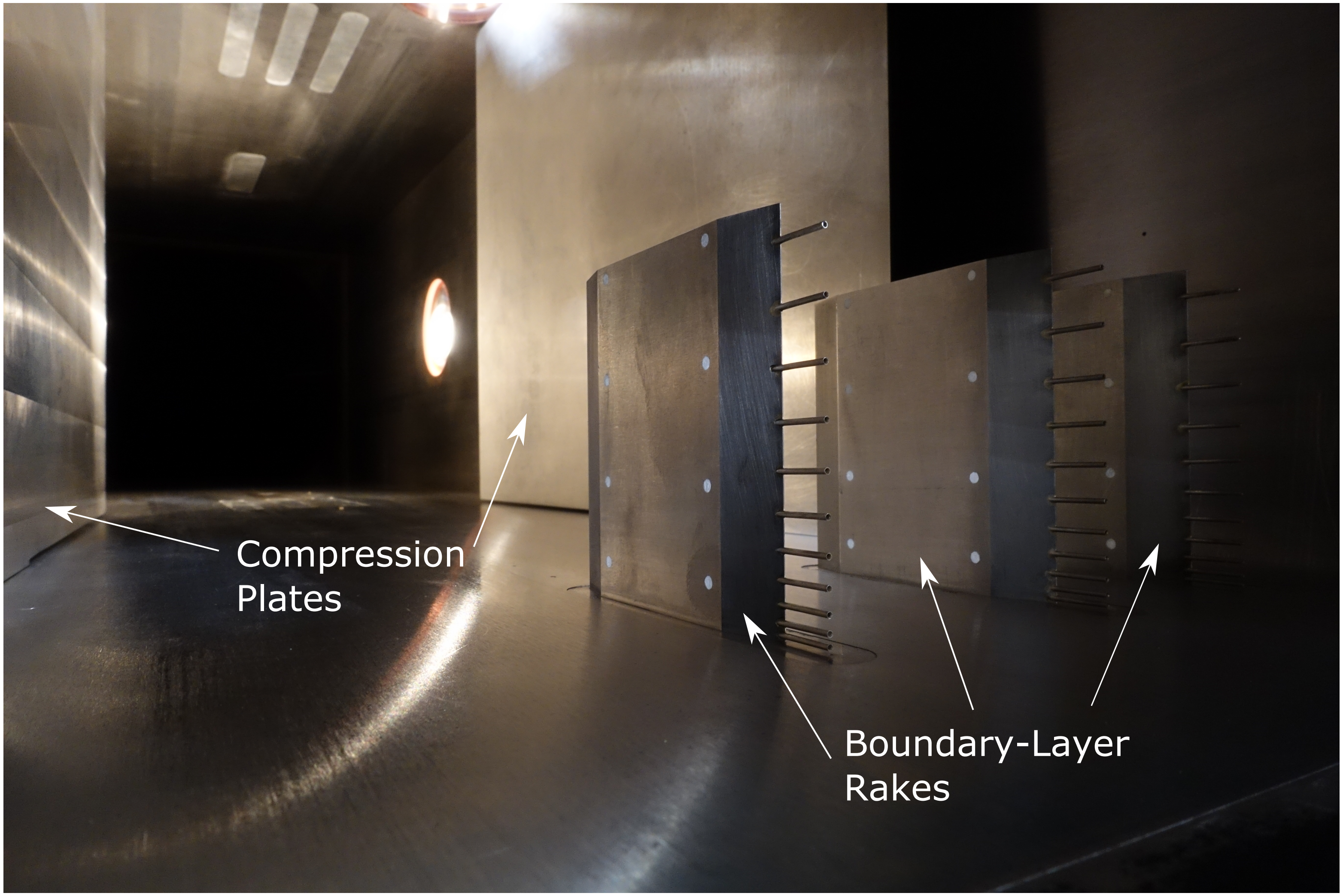

Fig. 11 Upstream boundary-layer rakes.

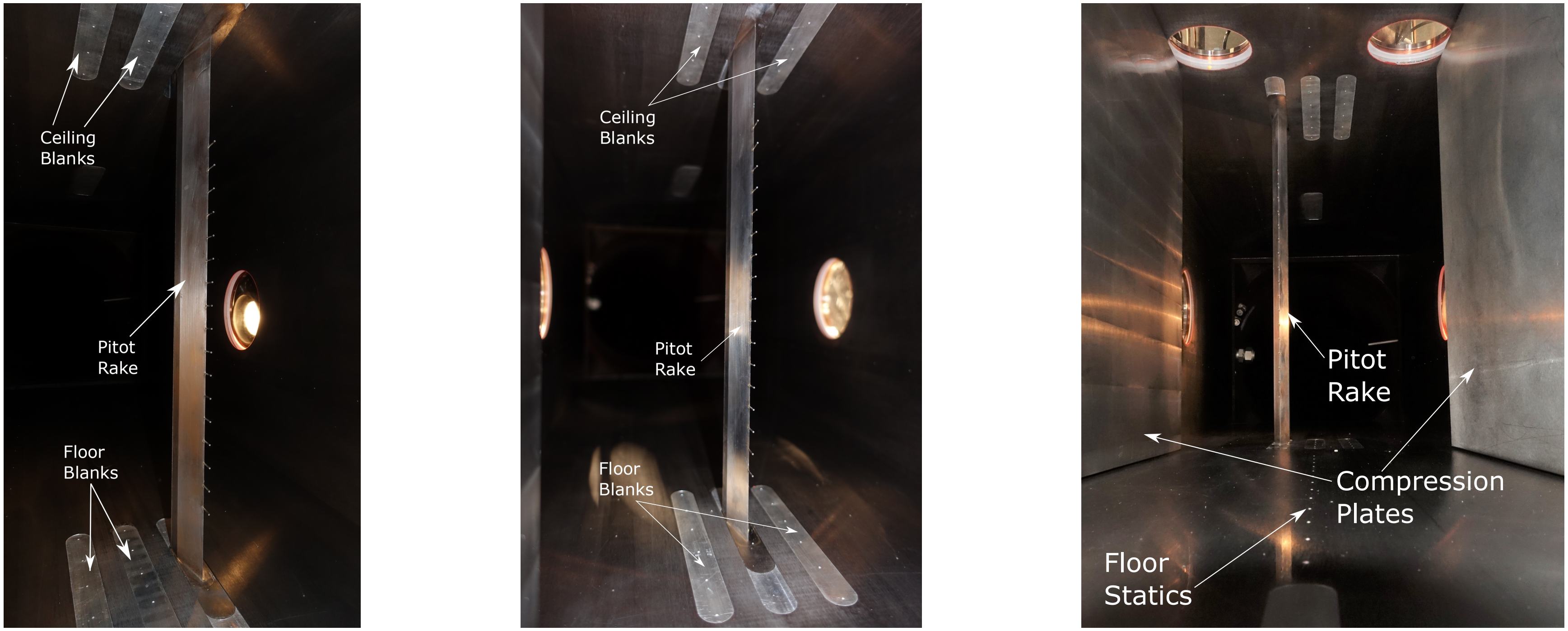

(a) Rake in port location.

(b) Rake in centerline location.

(c) Rake in starboard location.

Fig. 12 Downstream pitot rakes, rake blanks and static taps.

Fig. 13 Downstream static rake (uninstalled).

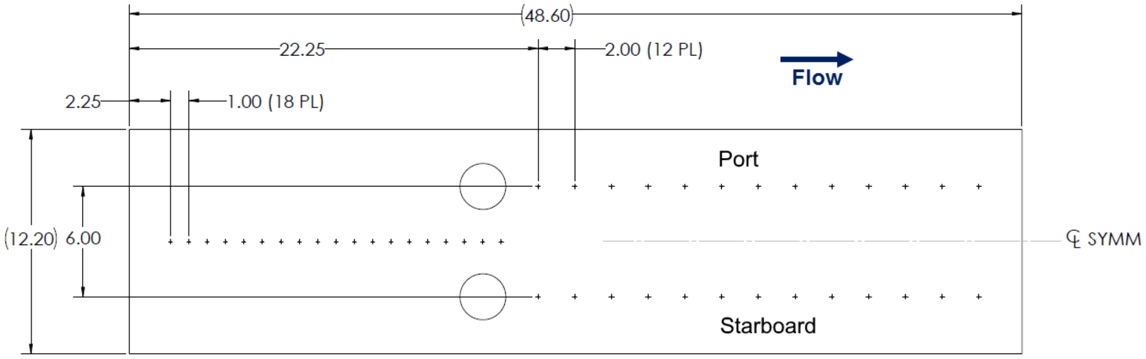

(a) Ceiling plate with rake blanks uninstalled. Location of three-inch diameter windows noted.

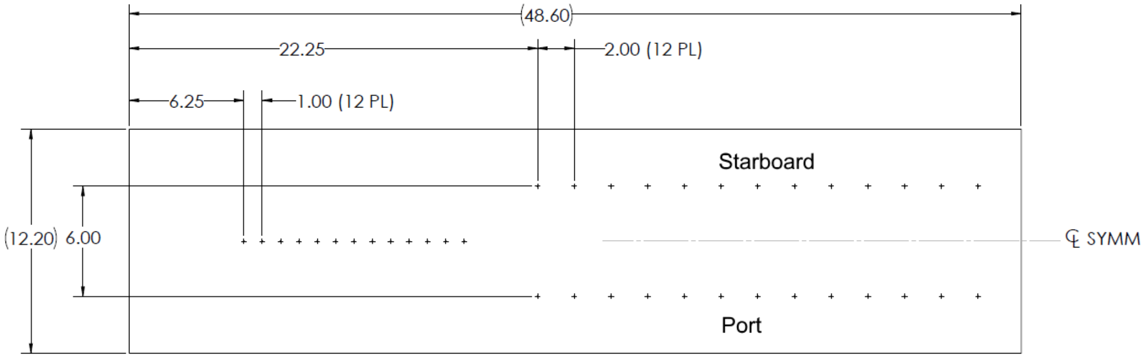

(b) Floor plate with rake blanks uninstalled.

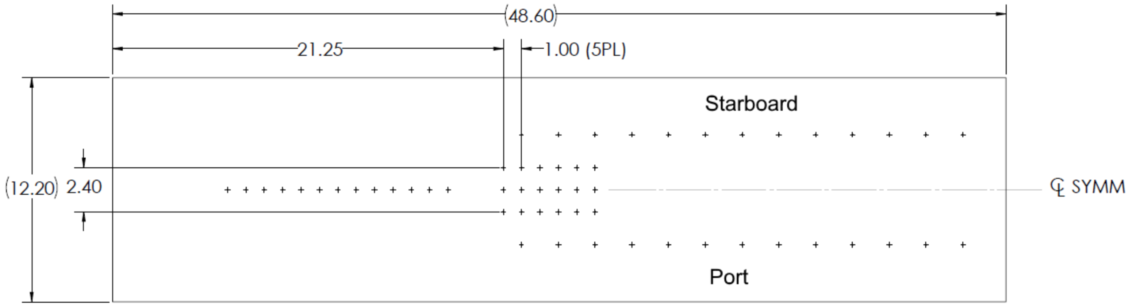

(c) Floor plate with rake blanks installed.

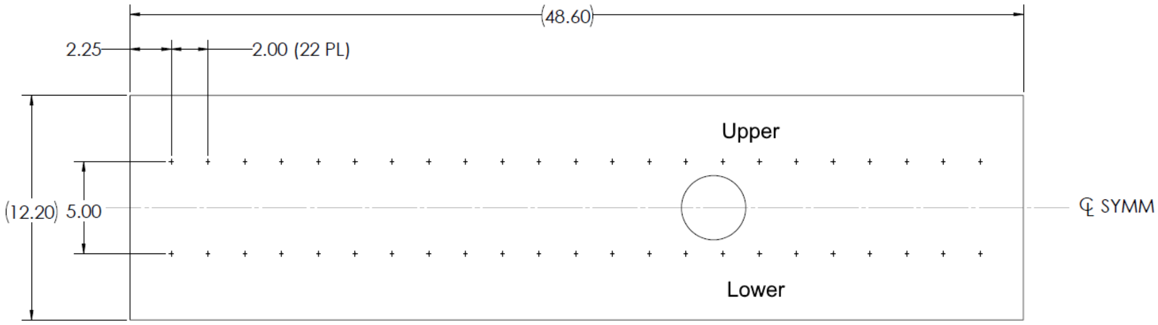

(d) Starboard sidewall plate (port sidewall is mirror image). Location of four-inch diameter window noted.

Fig. 14 Test section plates as viewed from flow surfaces. Windows and static pressure taps shown. Left edge of each plate corresponds to x = 2.95 inch. Except for rake blanks, pressure taps in (b) and (c) are identical.

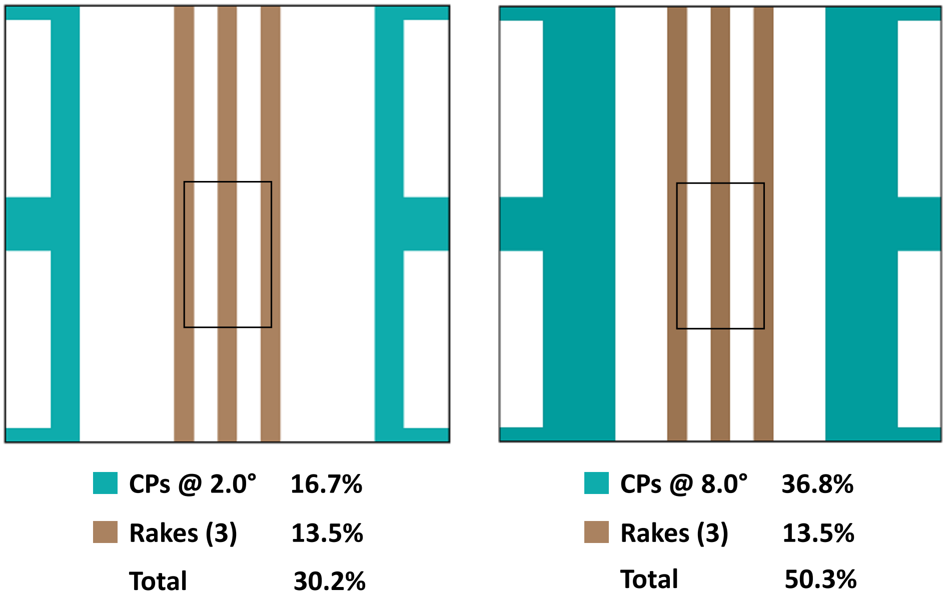

Fig. 15 Silhouettes of maximum blockage (i.e., three rakes) during attempts to start test section core flow (left, successful) and CP backside flow (right, unsuccessful). Removal of centerline rake permitted starting; however, testing with one rake at a time improved data quality. Black rectangle indicates notional high-q capture.

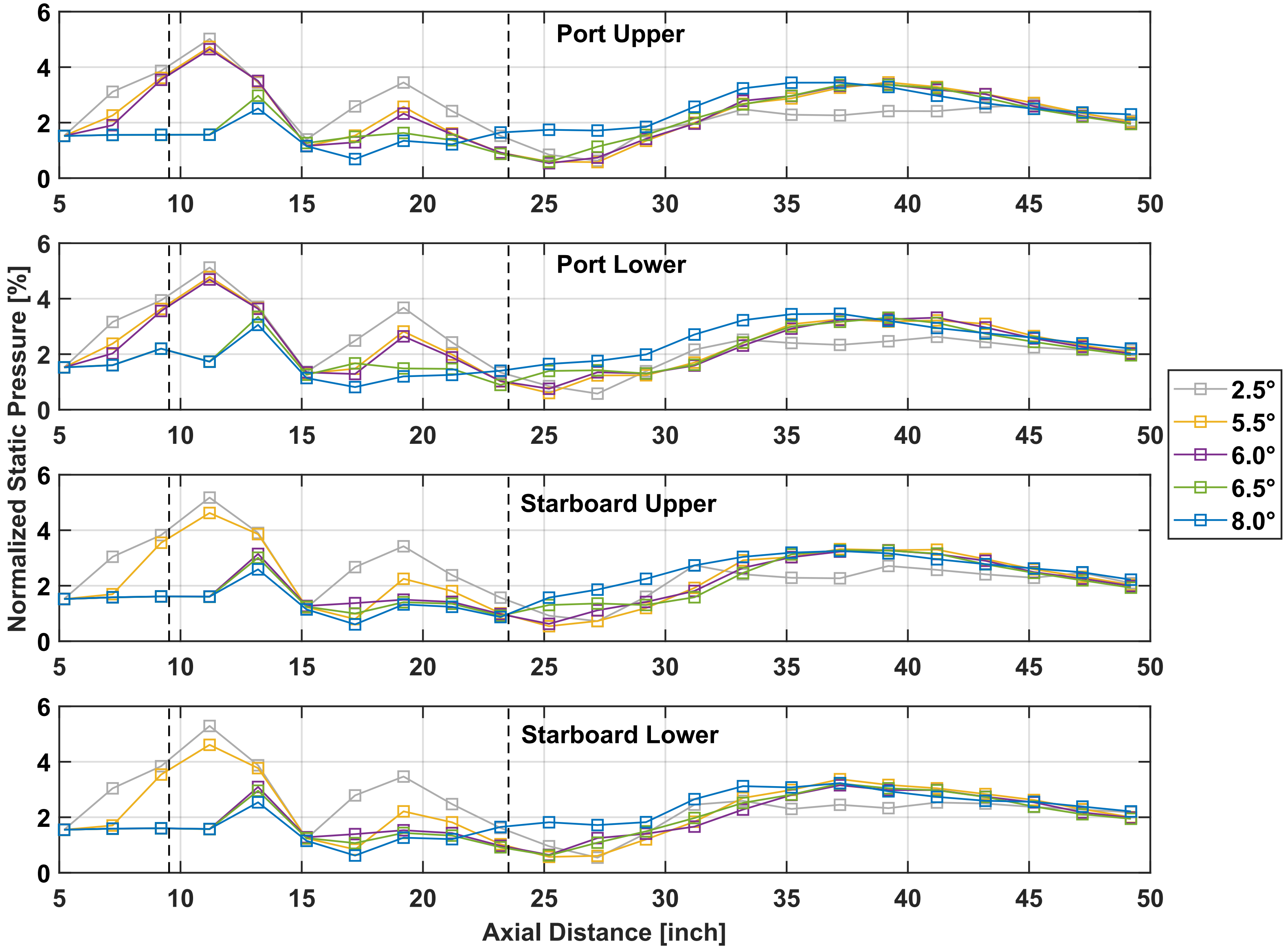

Fig. 16 Sidewall static pressures showing start/unstart behind compression plate. Dashed lines demarcate plate edges. Pressure normalized by p_{01}.

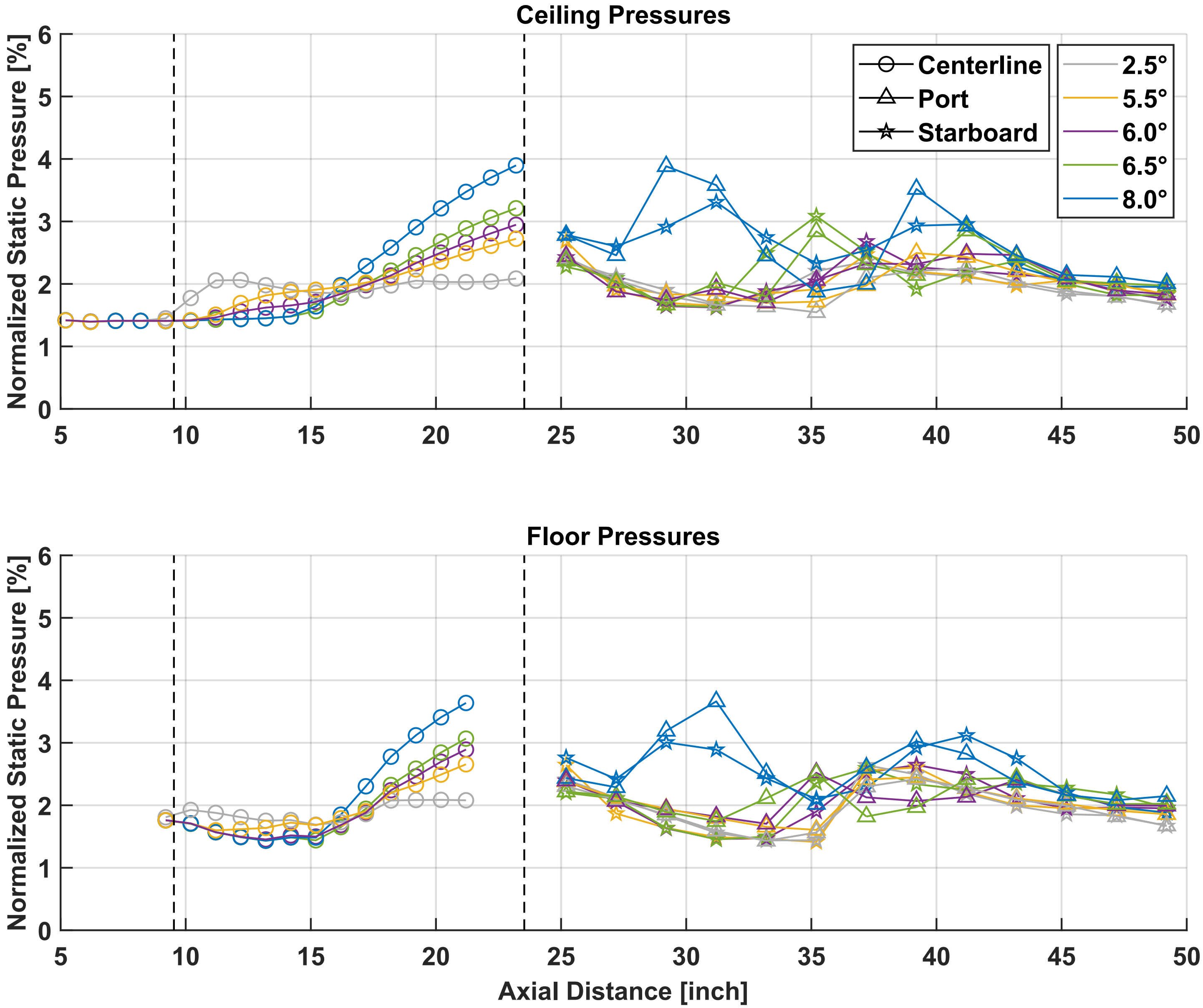

Fig. 17 Ceiling and floor static pressures showing start/unstart behind compression plate. Dashed lines demarcate plate edges. Pressure normalized by p_{01}.

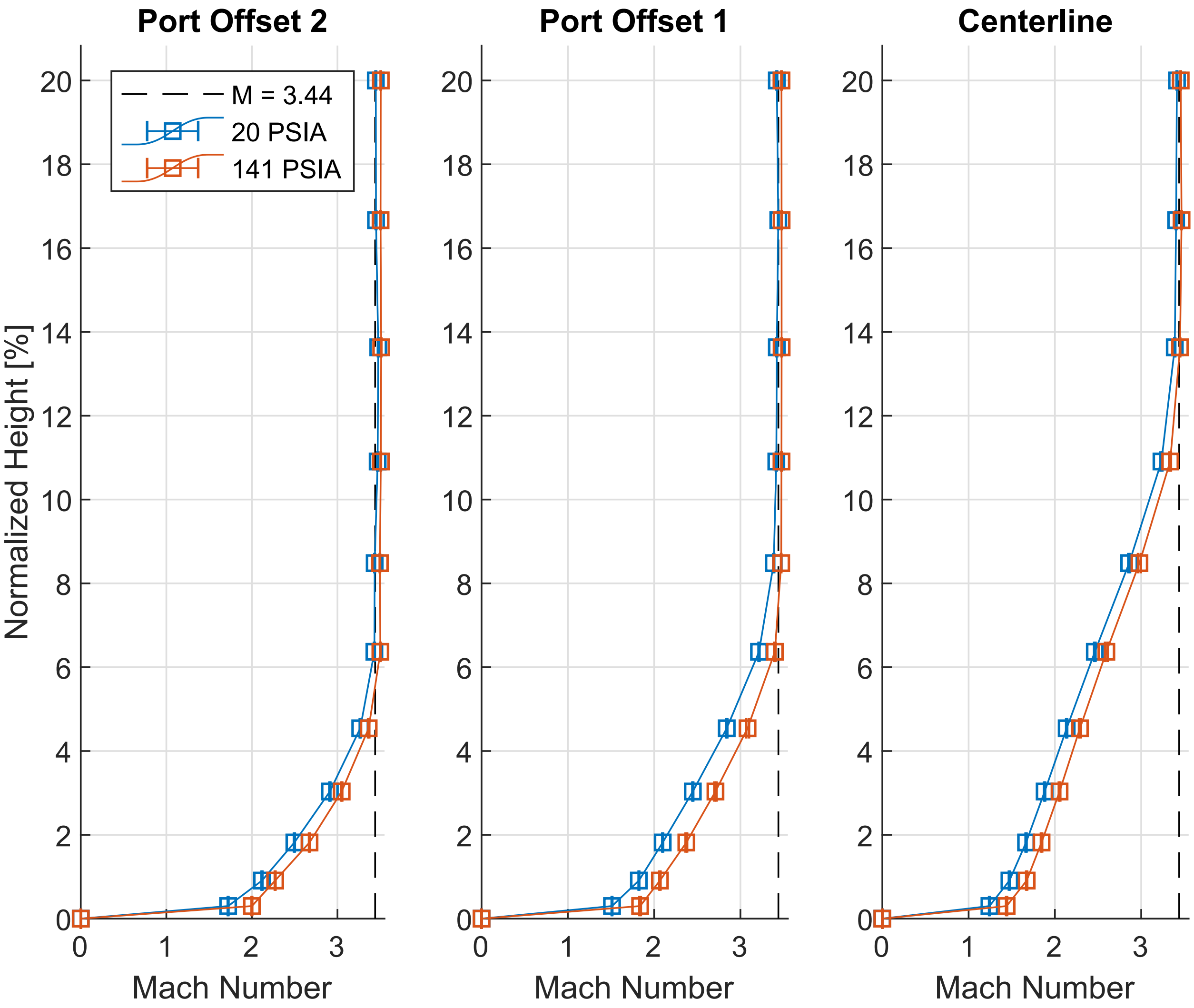

Fig. 18 Boundary-layer Mach profiles for lower and upper limit of tunnel total pressure. Height normalized by *h* (12.0 inches).

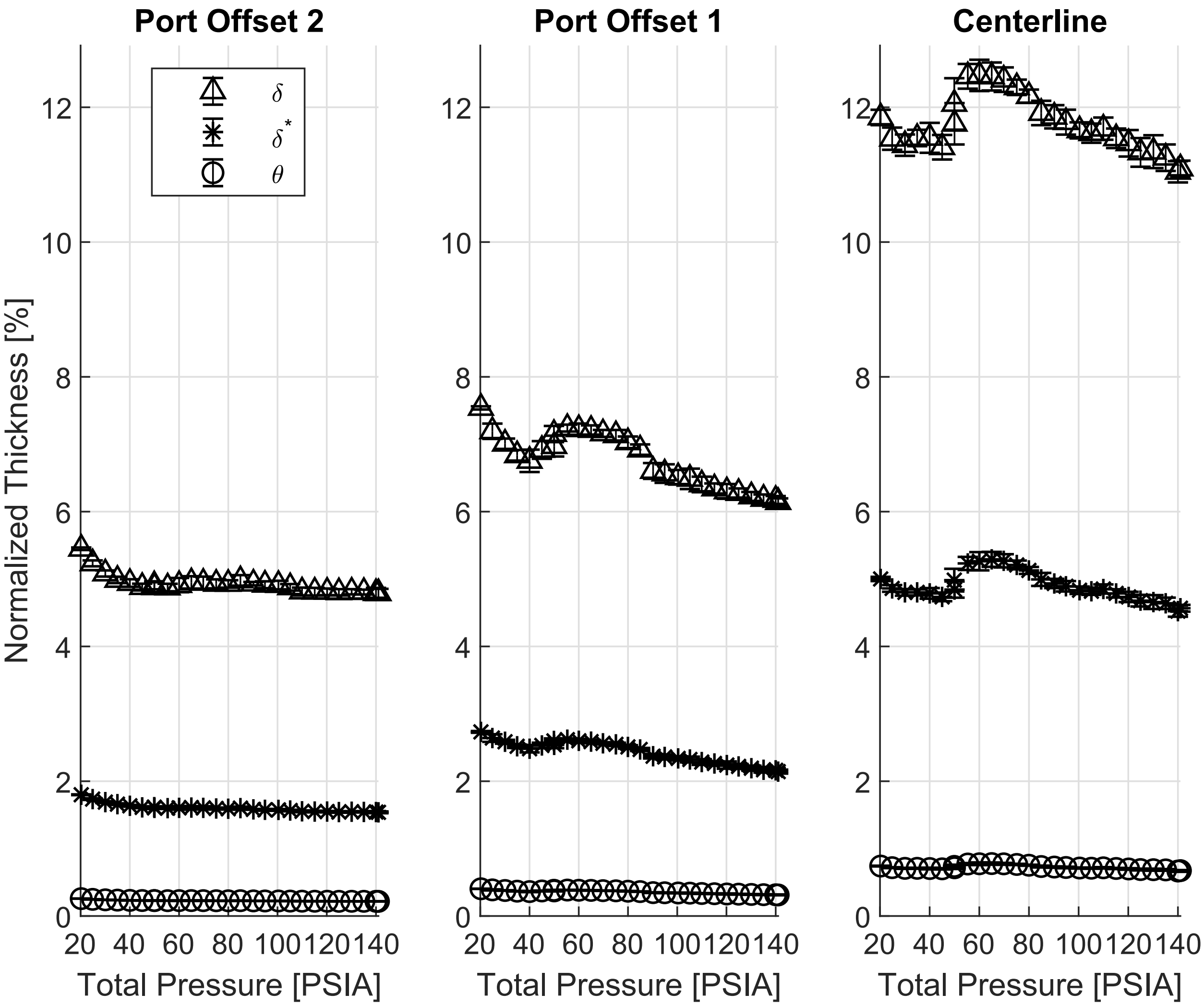

Fig. 19 Boundary-layer 99-percent (triangles), displacement (asterisks) and momentum (circles) thicknesses. Height normalized by *h* (12.0 inches).

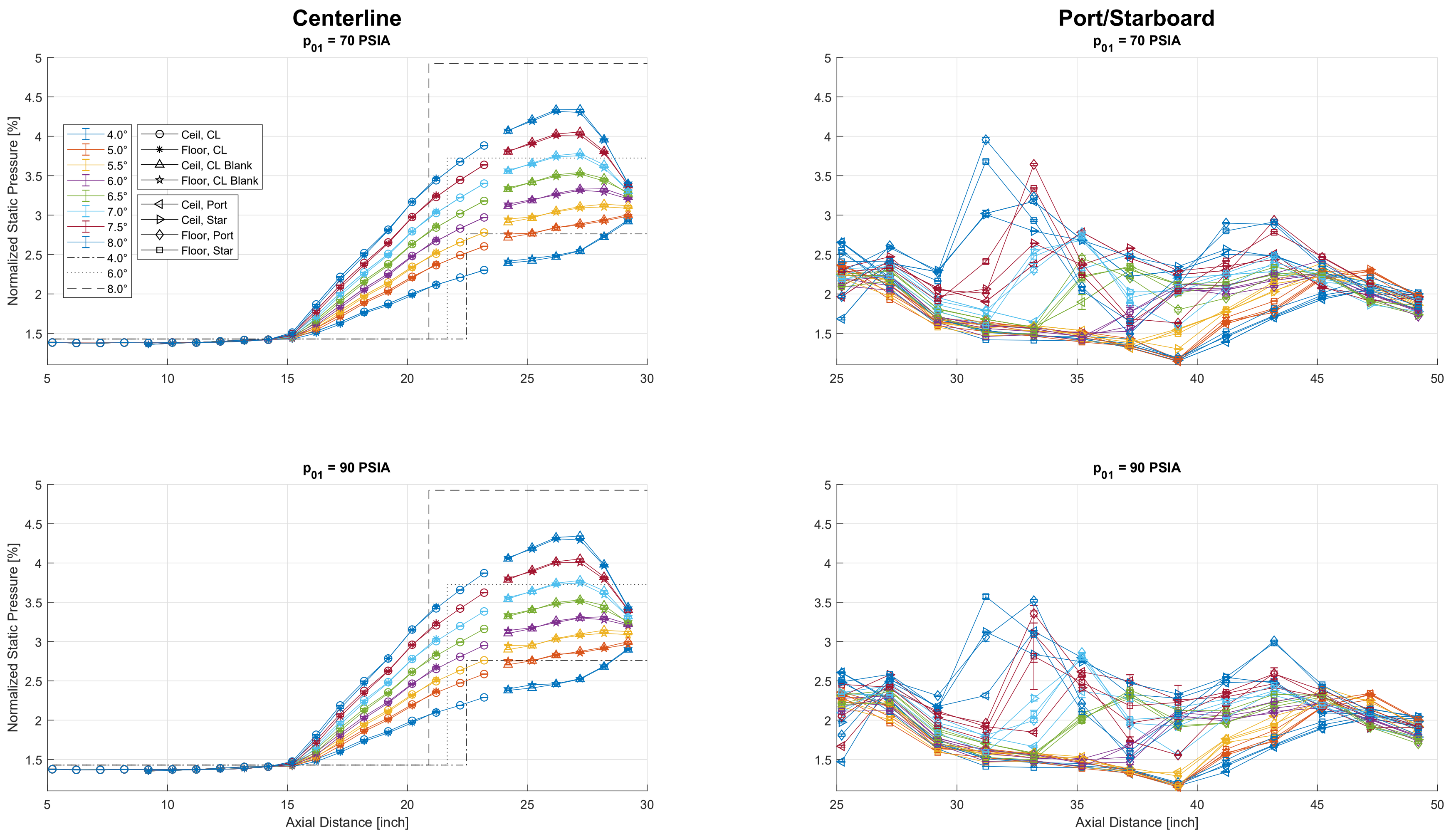

Fig. 20 Ceiling/floor static pressure distribution as function of plate angle and tunnel total pressure (70–90 psia). Pressure normalized by p_{01}.

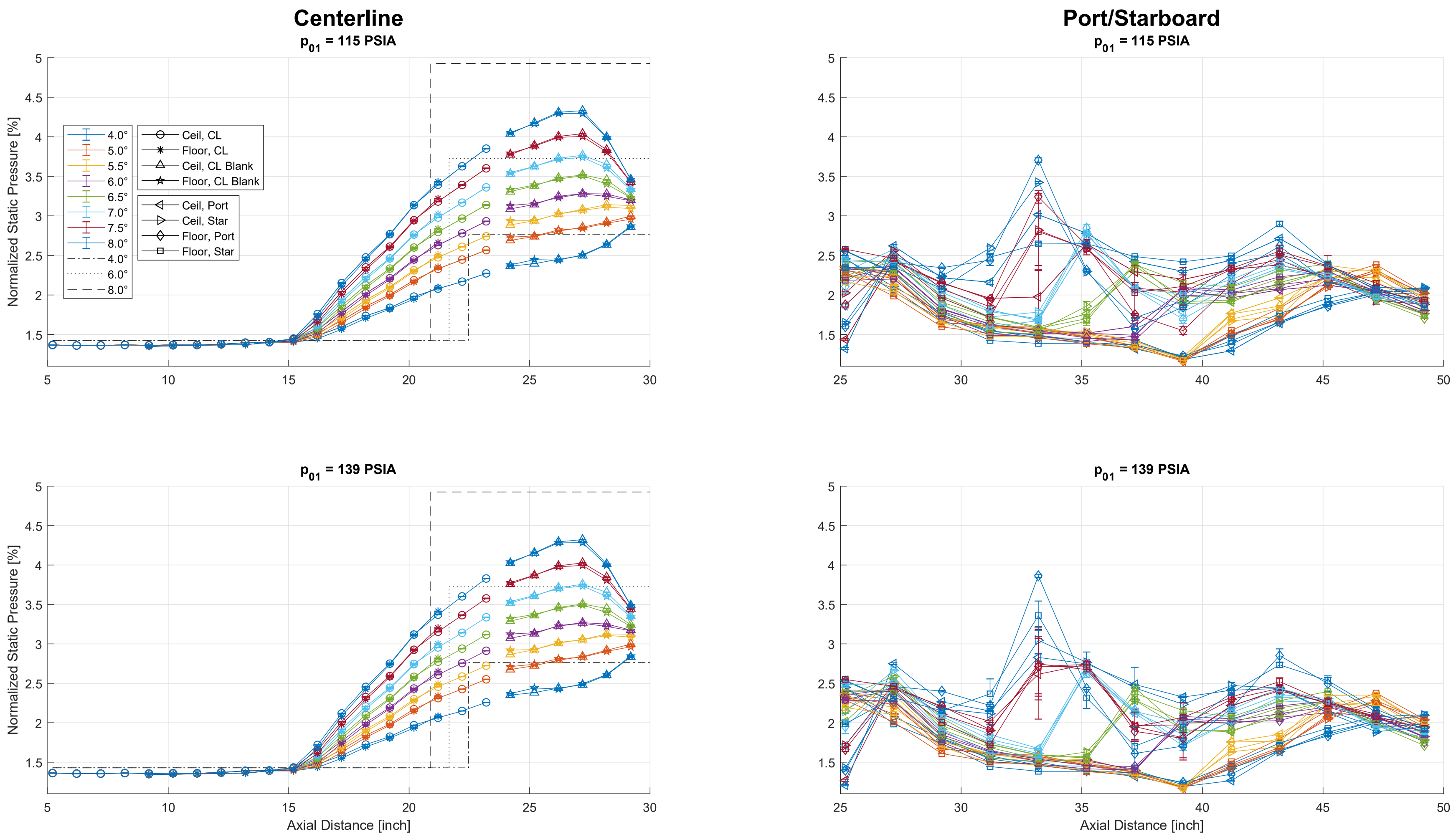

Fig. 21 Ceiling/floor static pressure distribution as function of plate angle and tunnel total pressure (115–139 psia). Pressure normalized by p_{01}.

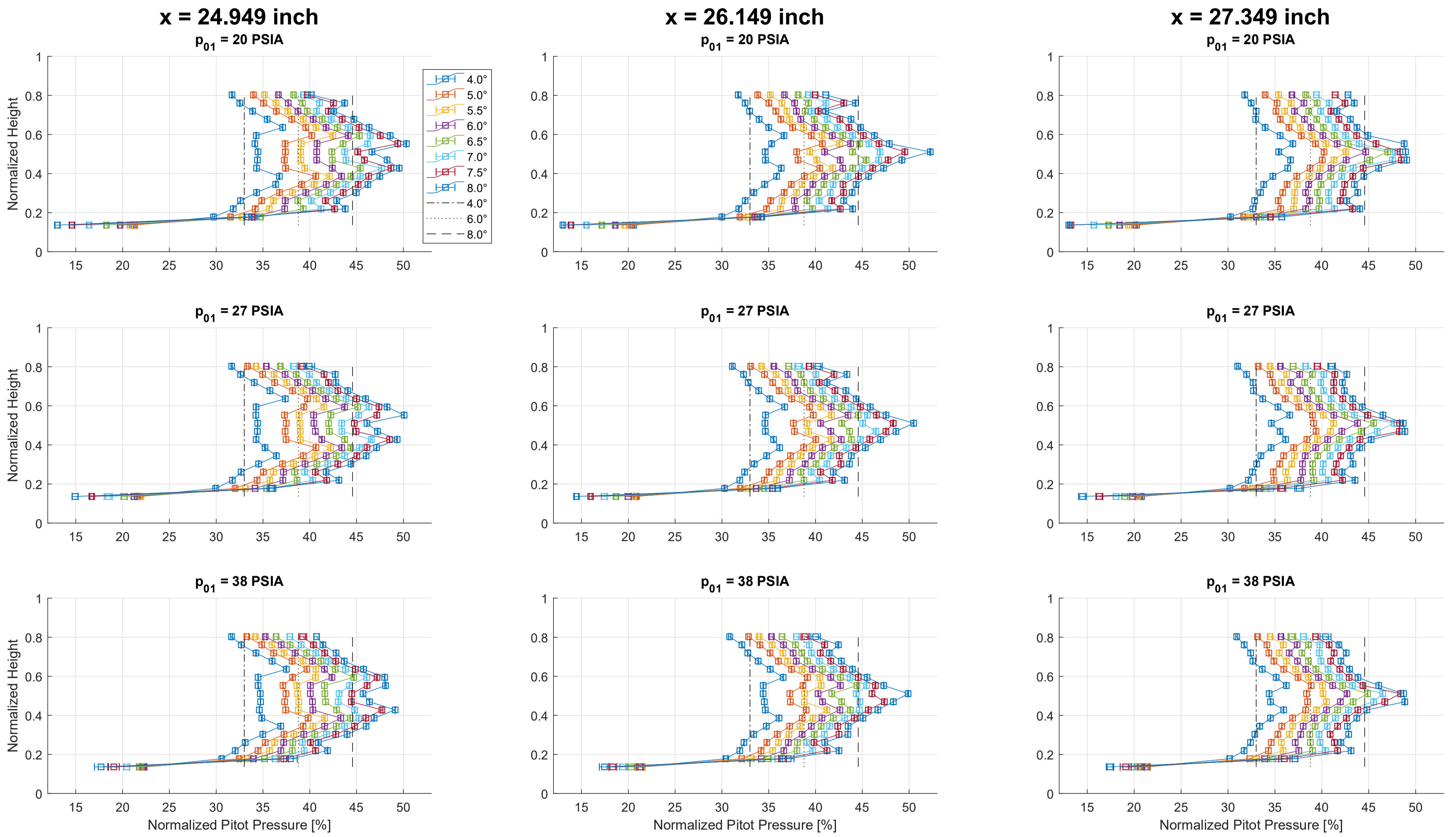

Fig. 22 Centerline pitot pressure profile as function of plate angle, axial station and tunnel total pressure (20–38 psia). Pressure and height normalized by p_{01} and h, respectively.

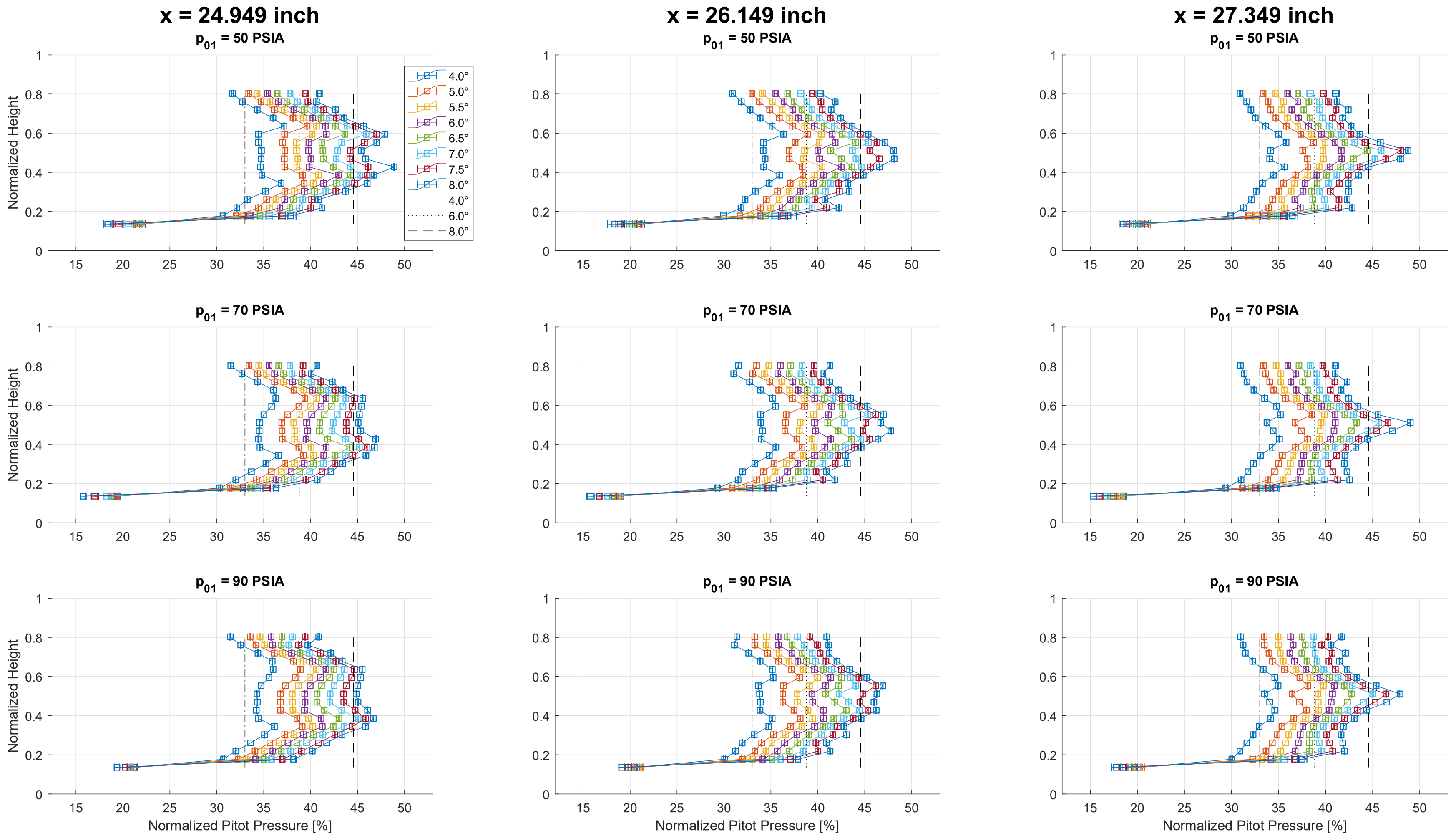

Fig. 23 Centerline pitot pressure profile as function of plate angle, axial station and tunnel total pressure (50–90 psia). Pressure and height normalized by p_{01} and h, respectively.

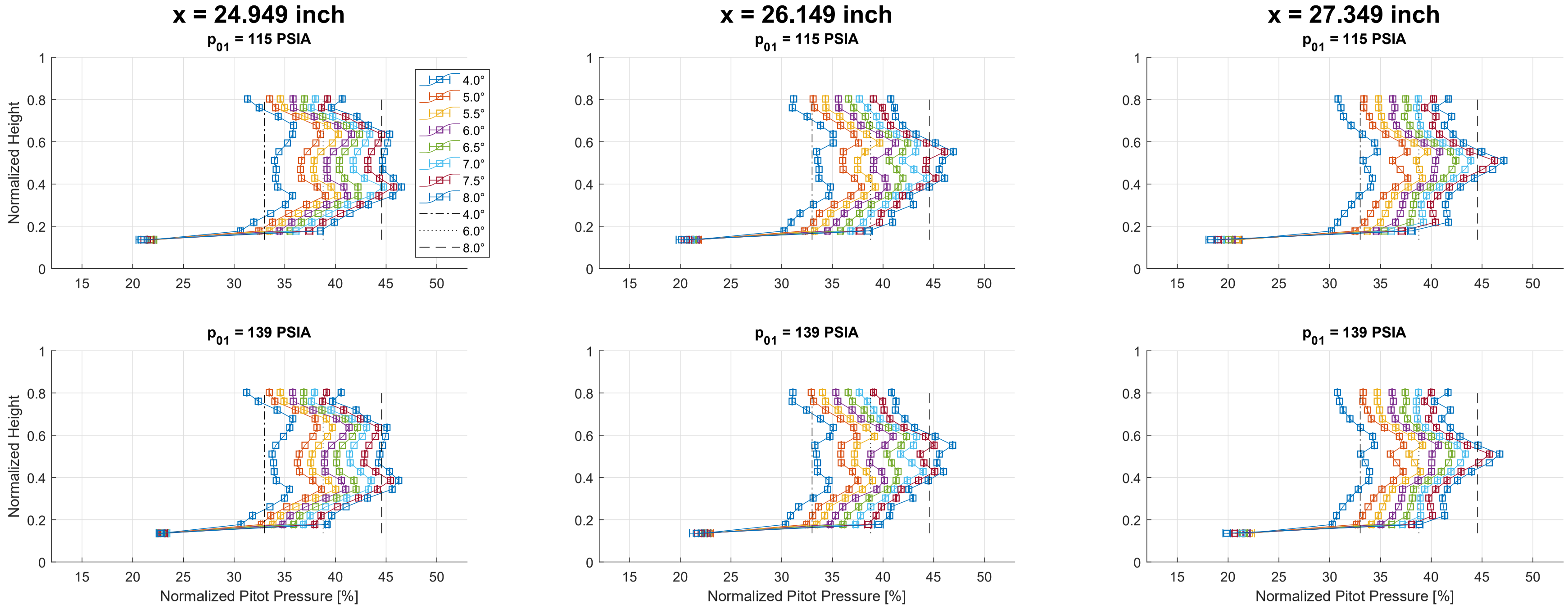

Fig. 24 Centerline pitot pressure profile as function of plate angle, axial station and tunnel total pressure (115–139 psia). Pressure and height normalized by p_{01} and h, respectively.

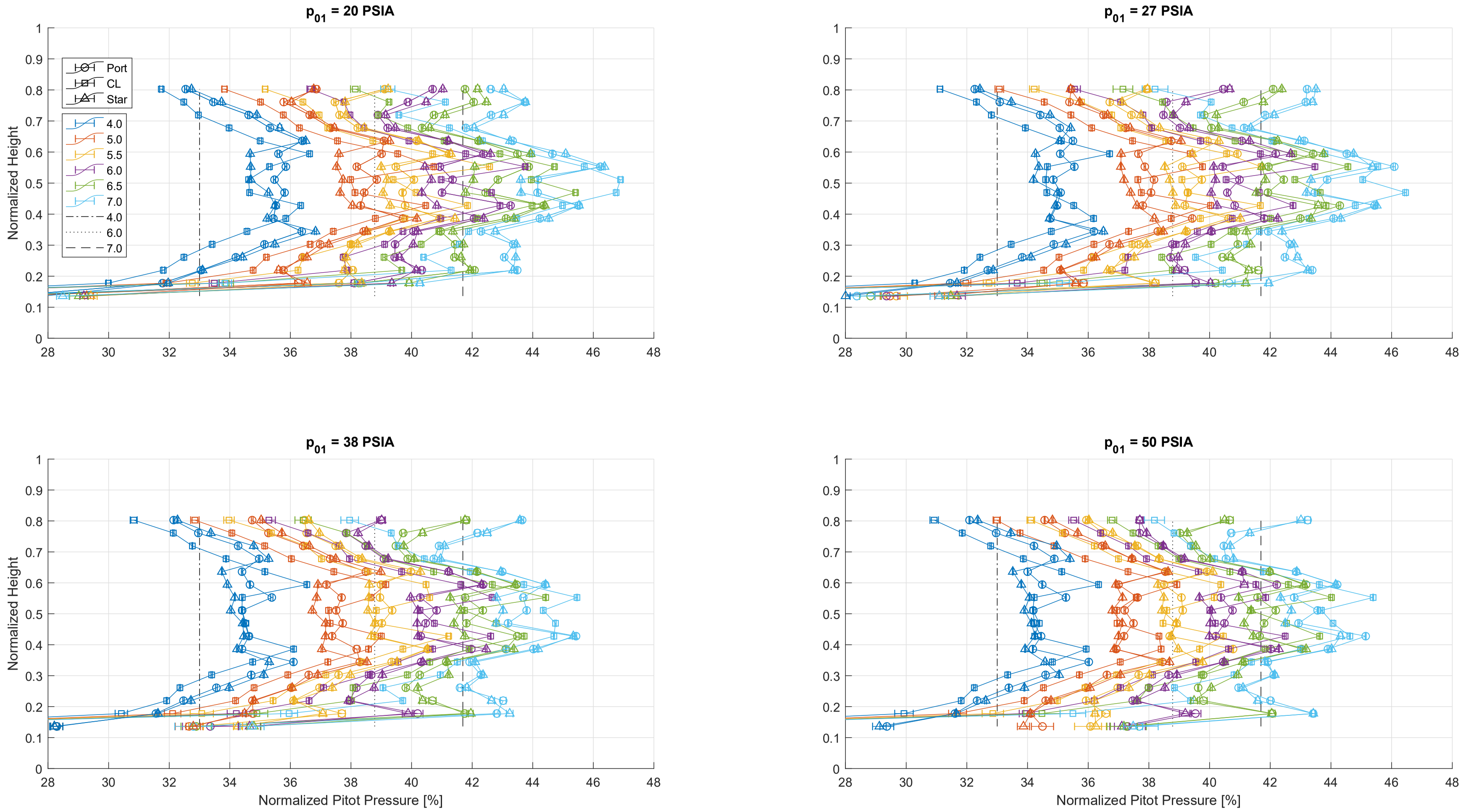

Fig. 25 Spanwise comparison of pitot pressure profiles for varying plate angle and tunnel total pressure (20–50 psia), but fixed axial station (x = 26.149 inch). Pressure and height normalized by p_{01} and h, respectively.

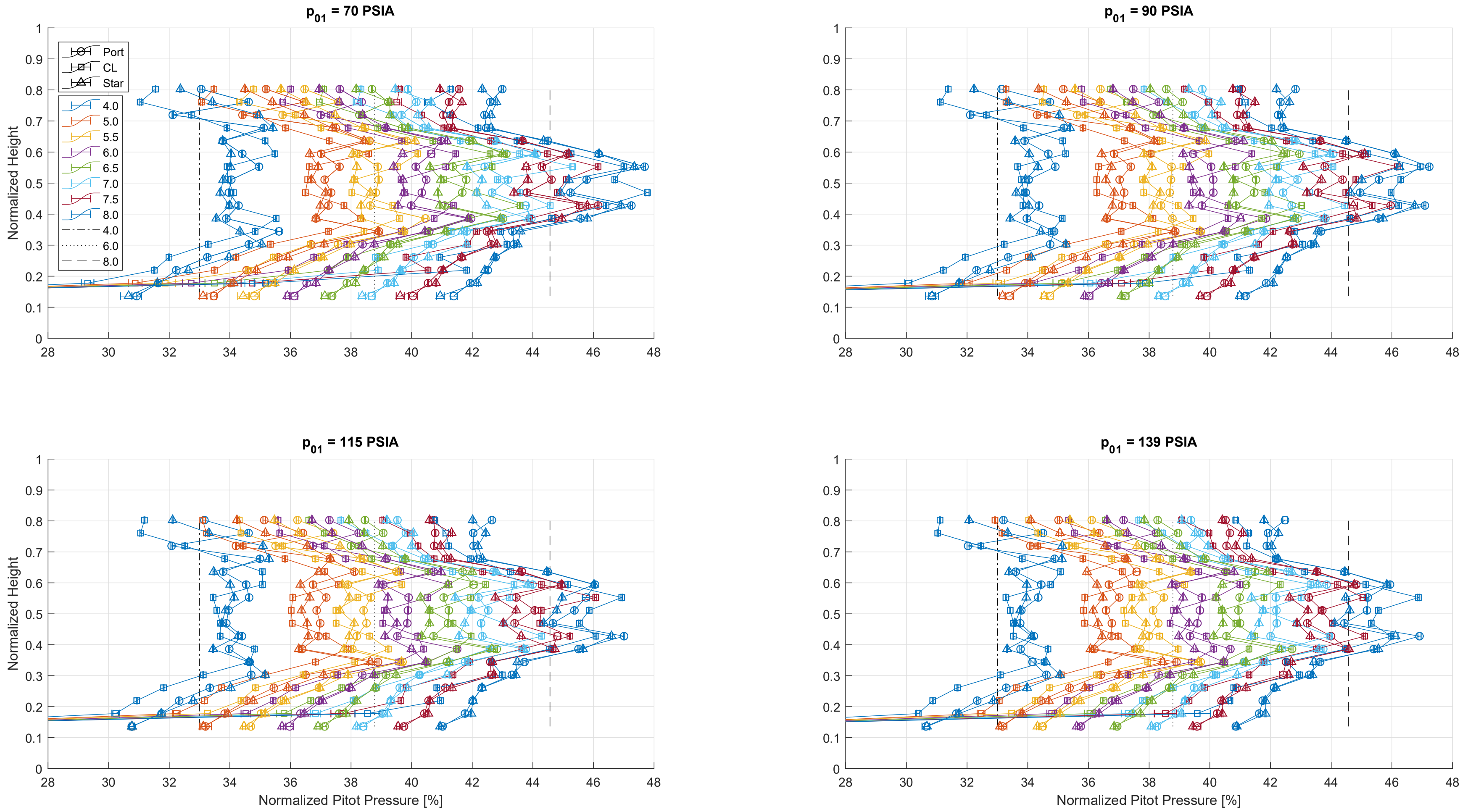

Fig. 26 Spanwise comparison of pitot pressure profiles for varying plate angle and tunnel total pressure (70–139 psia), but fixed axial station (x = 26.149 inch). Pressure and height normalized by p_{01} and h, respectively.

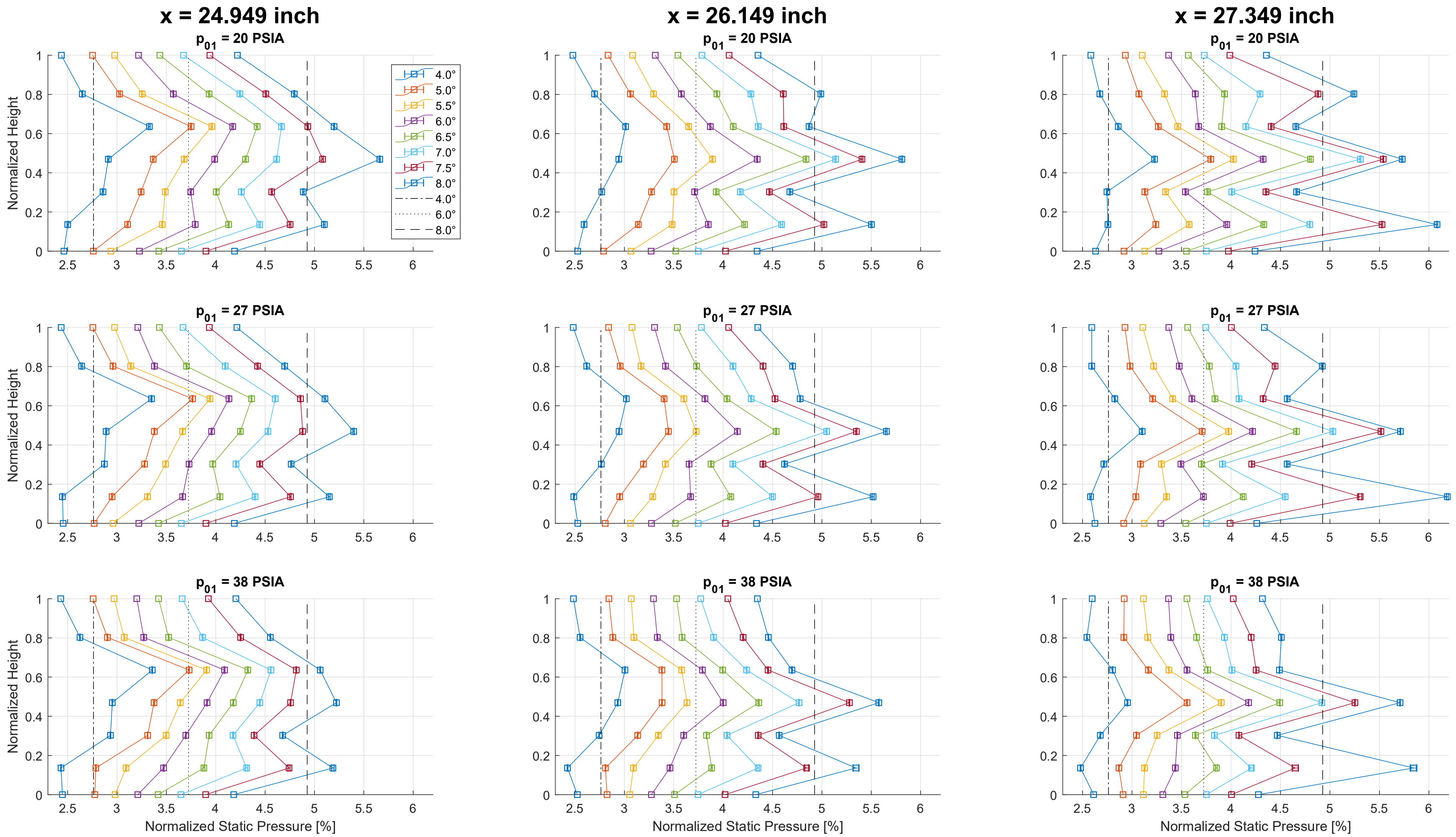

Fig. 27 Centerline static pressure profile as function of plate angle, axial station and tunnel total pressure (20–38 psia). Pressure and height normalized by p_{01} and h, respectively.

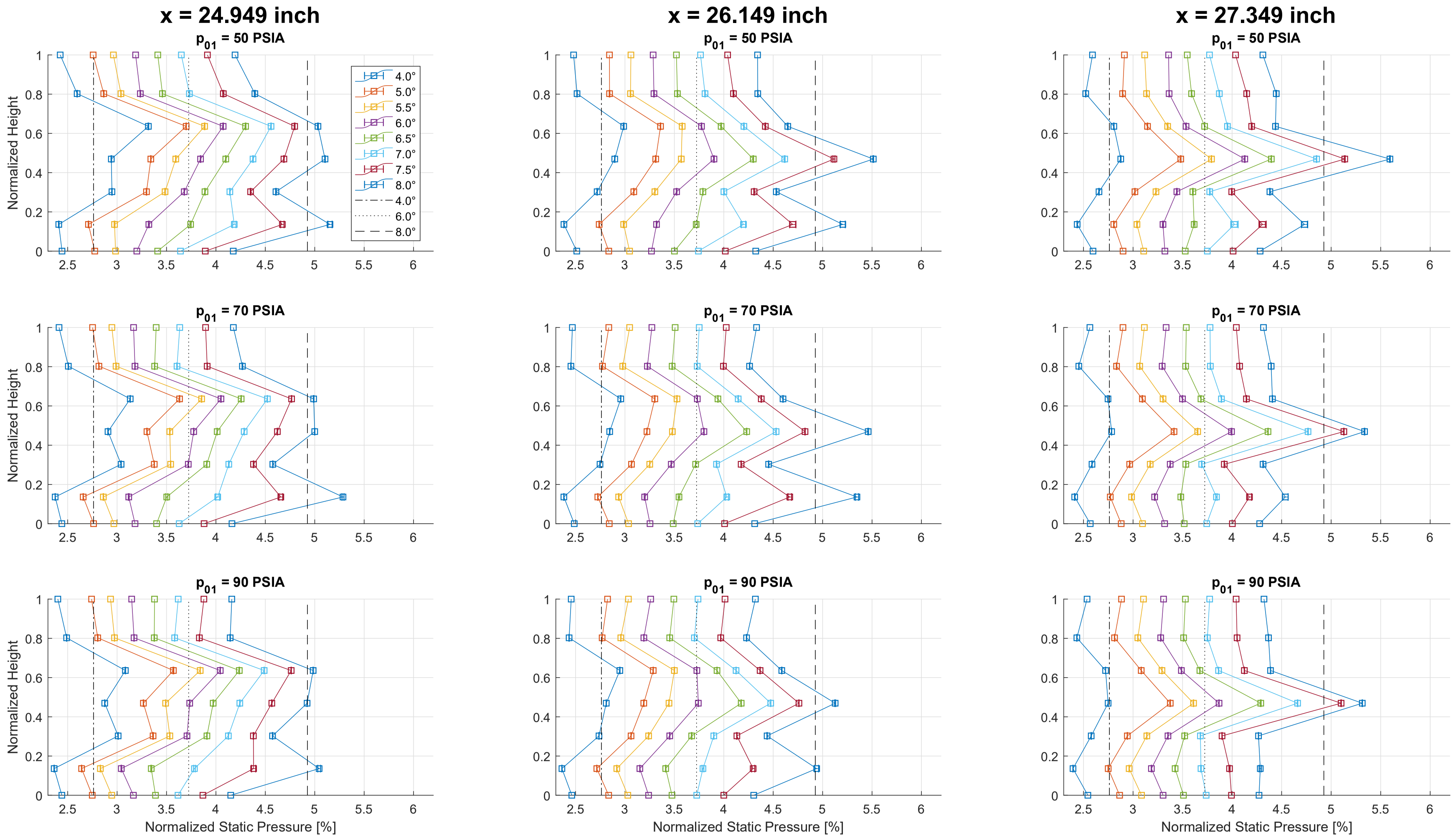

Fig. 28 Centerline static pressure profile as function of plate angle, axial station and tunnel total pressure (50–90 psia). Pressure and height normalized by p_{01} and h, respectively.

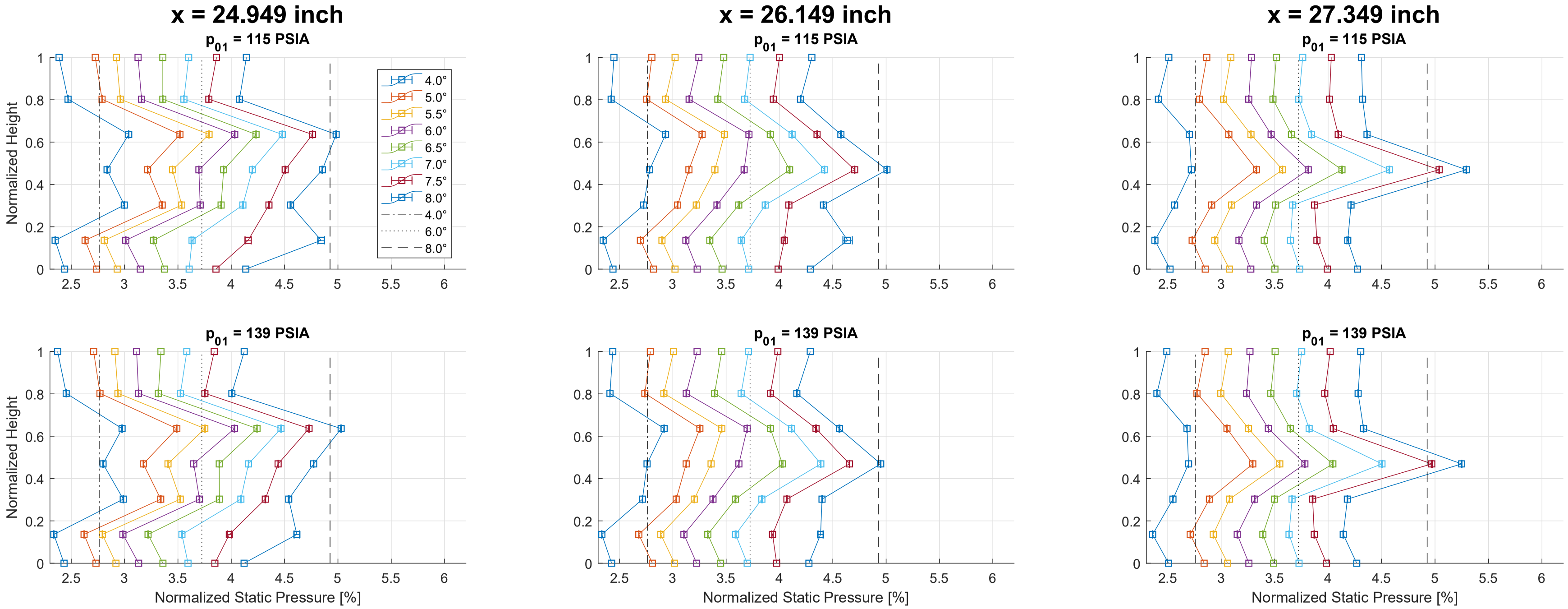

Fig. 29 Centerline static pressure profile as function of plate angle, axial station and tunnel total pressure (115–139 psia). Pressure and height normalized by p_{01} and h, respectively.

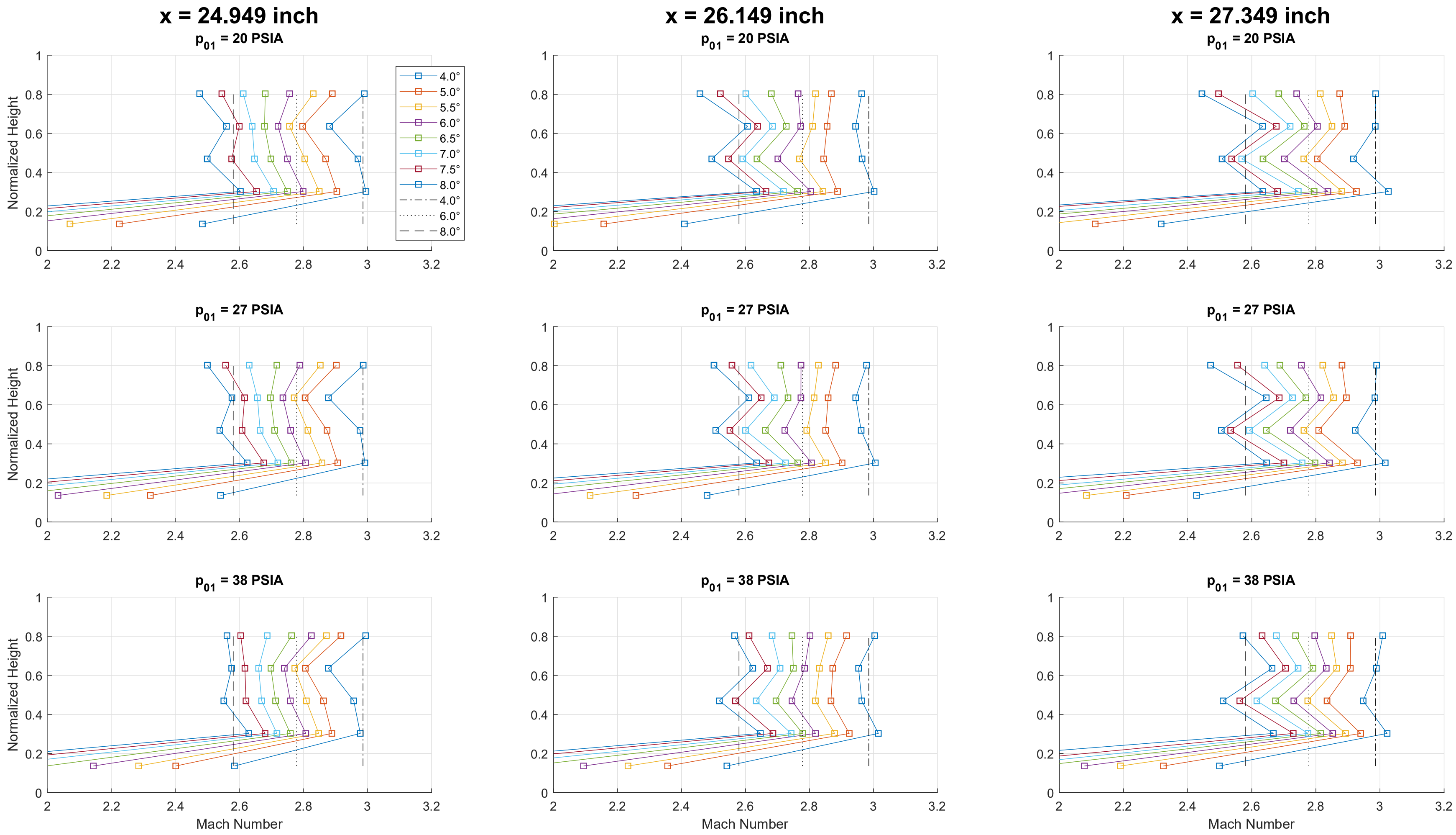

Fig. 30 Centerline Mach profile (calculated) as function of plate angle, axial station and tunnel total pressure (20–38 psia). Height normalized by *h*.

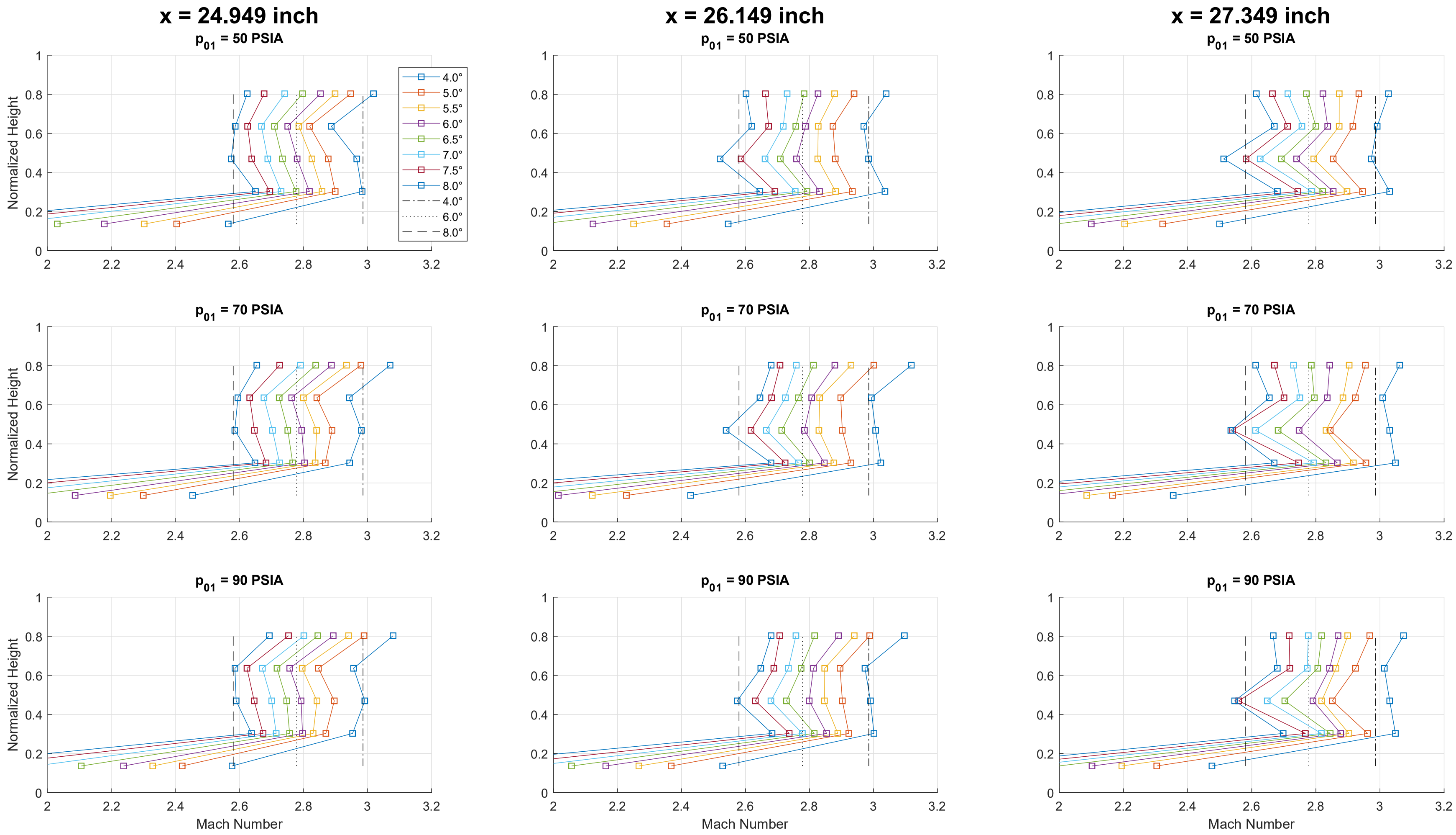

Fig. 31 Centerline Mach profile (calculated) as function of plate angle, axial station and tunnel total pressure (50–90 psia). Height normalized by *h*.

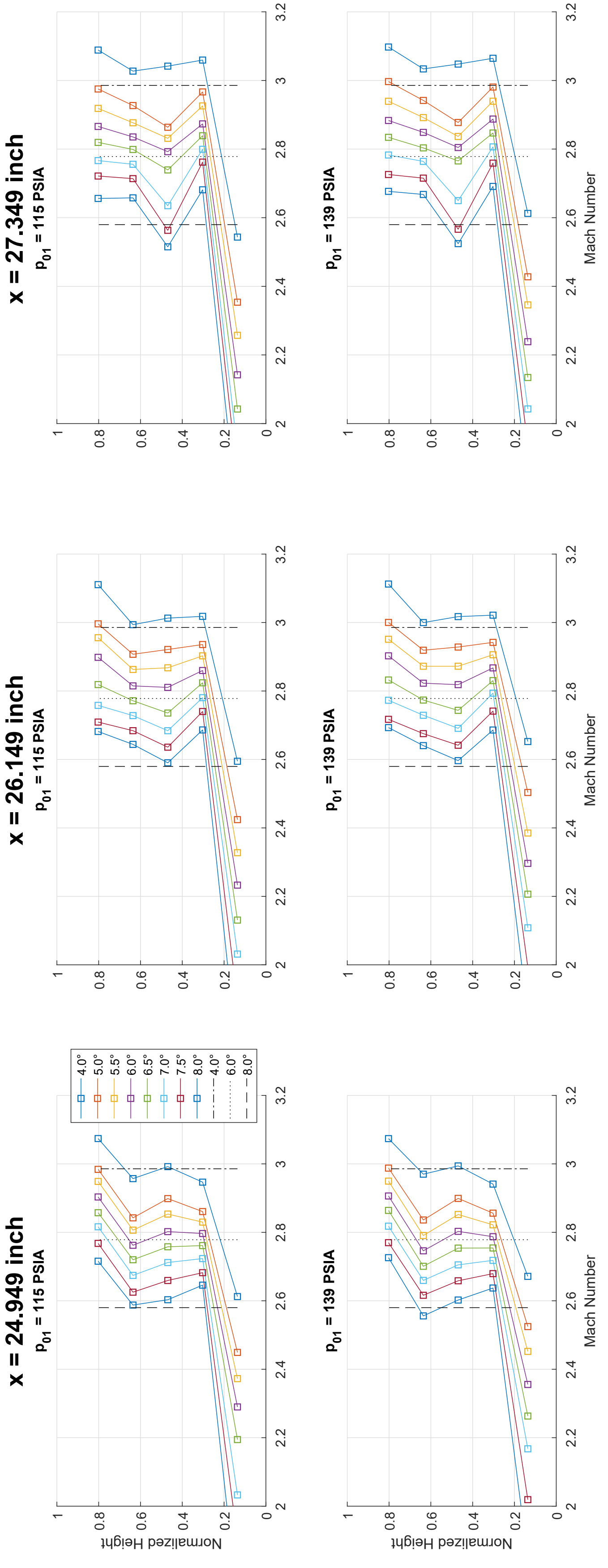

Fig. 32 Centerline Mach profile (calculated) as function of plate angle, axial station and tunnel total pressure (115–139 psia). Height normalized by *h*.

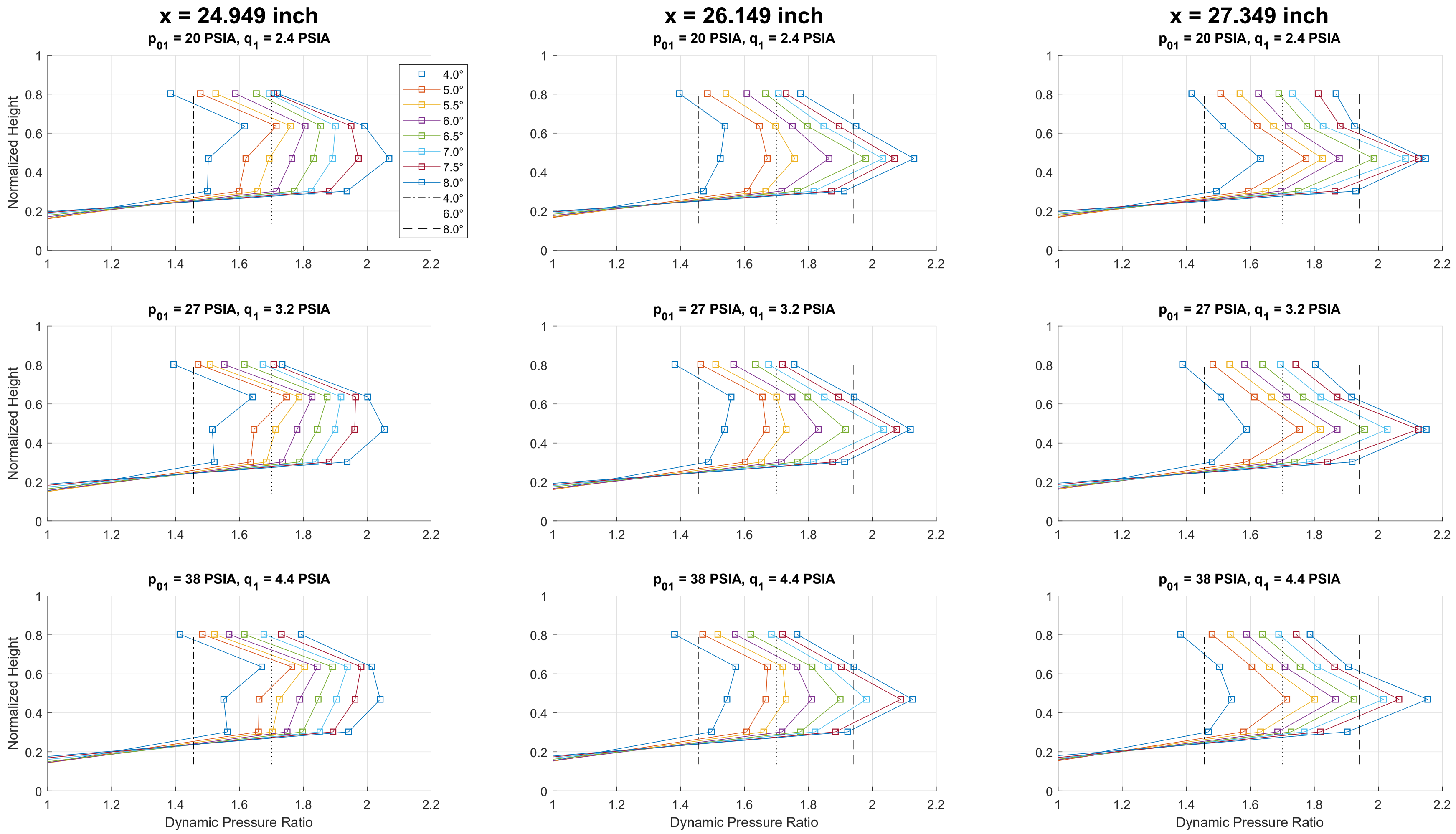

Fig. 33 Centerline dynamic pressure profile (calculated) as function of plate angle, axial station and tunnel total pressure (20–38 psia). Ratio based on q_1. Height normalized by h.

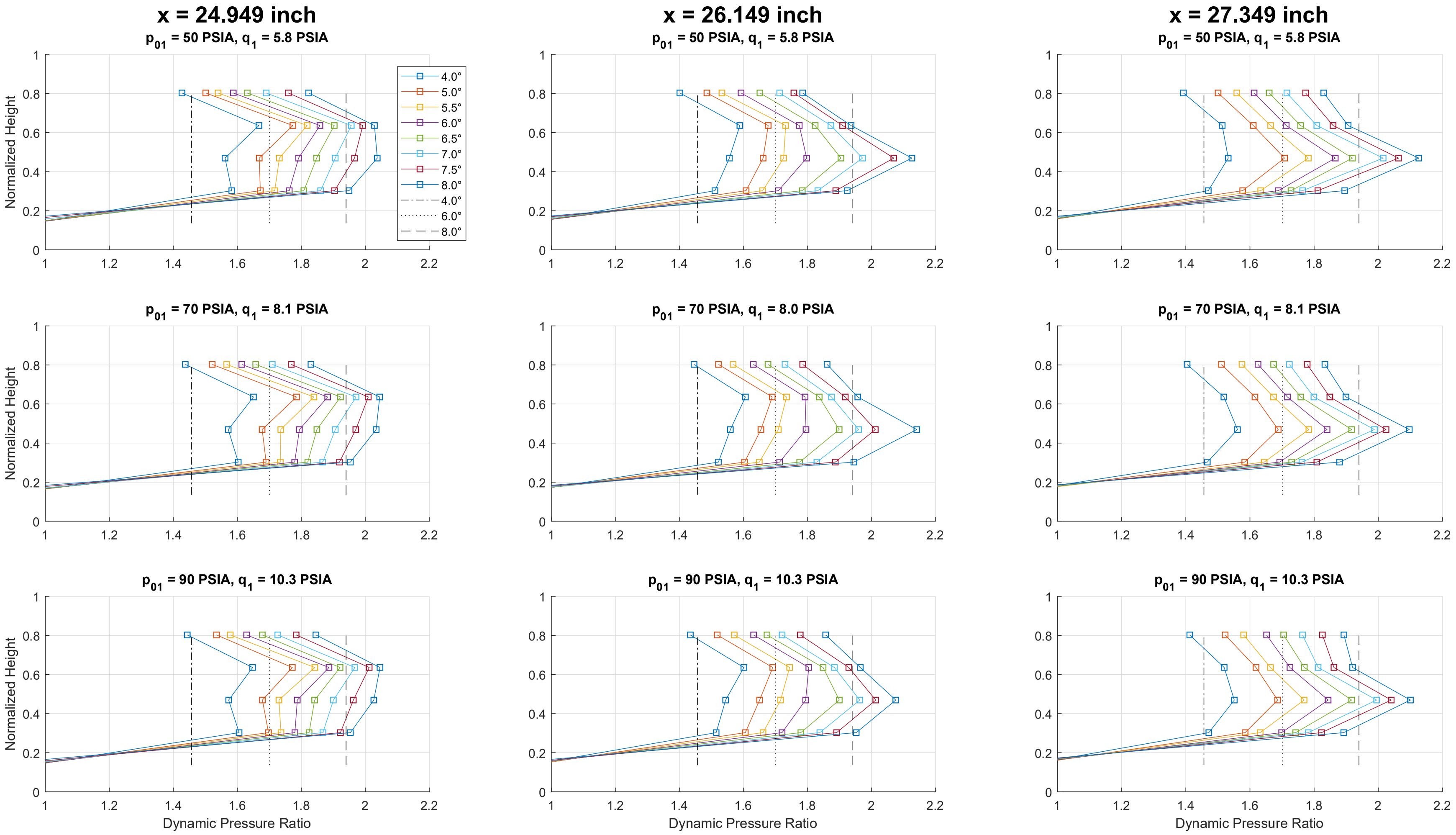

Fig. 34 Centerline dynamic pressure profile (calculated) as function of plate angle, axial station and tunnel total pressure (50–90 psia). Ratio based on q_1. Height normalized by h.

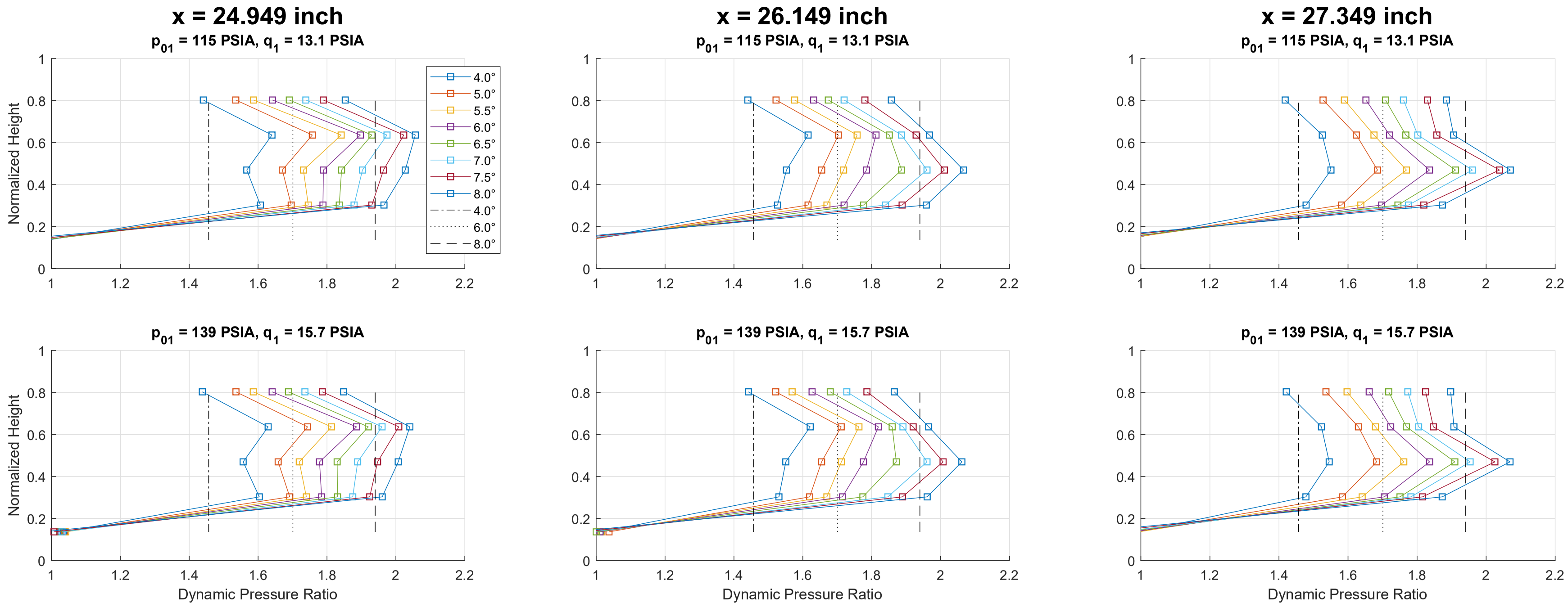

Fig. 35 Centerline dynamic pressure profile (calculated) as function of plate angle, axial station and tunnel total pressure (115–139 psia). Ratio based on q_1. Height normalized by h.

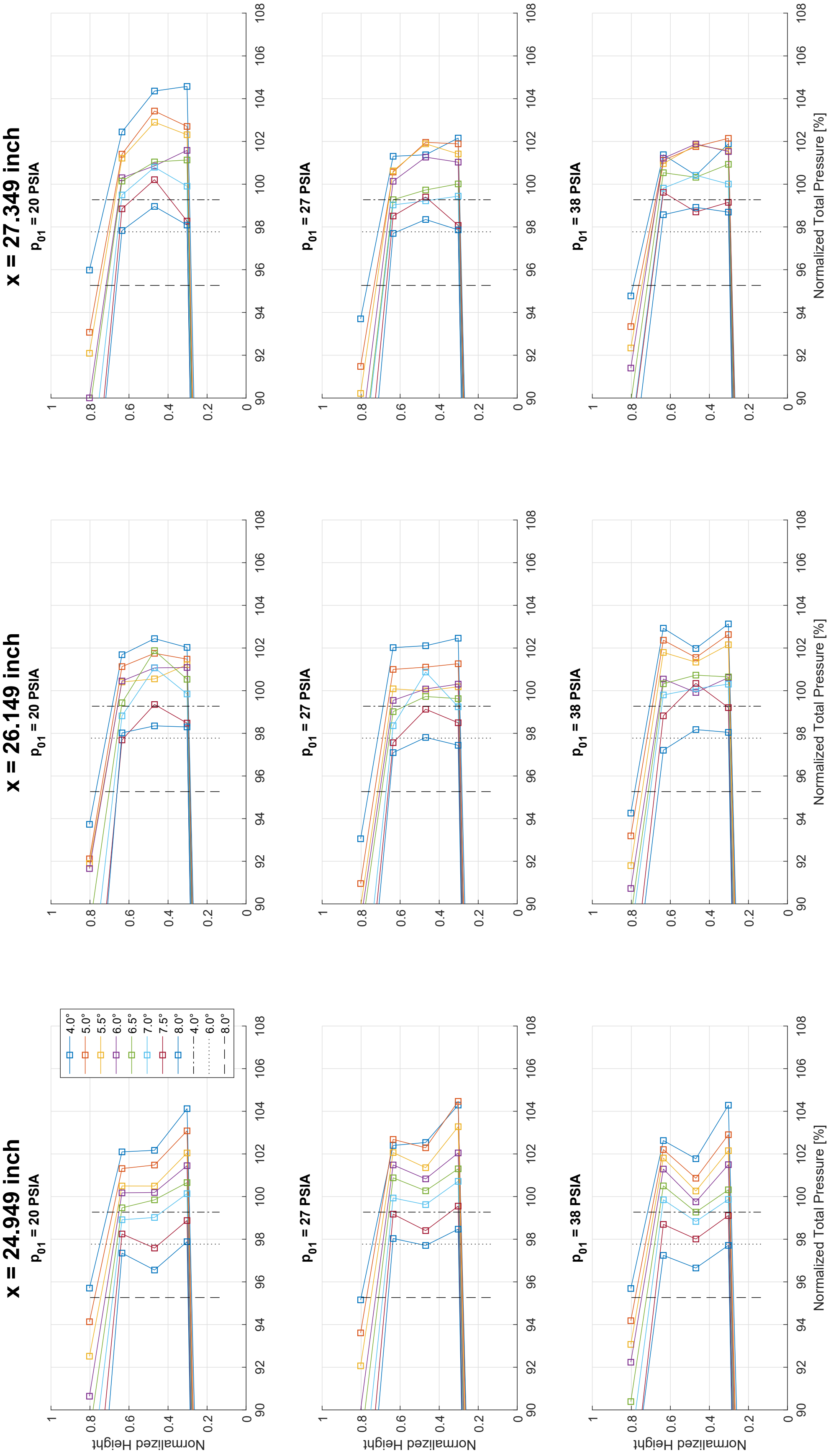

Fig. 36 Centerline total pressure profile (calculated) as function of plate angle, axial station and tunnel total pressure (20–38 psia). Pressure and height normalized by p_{01} and h, respectively.

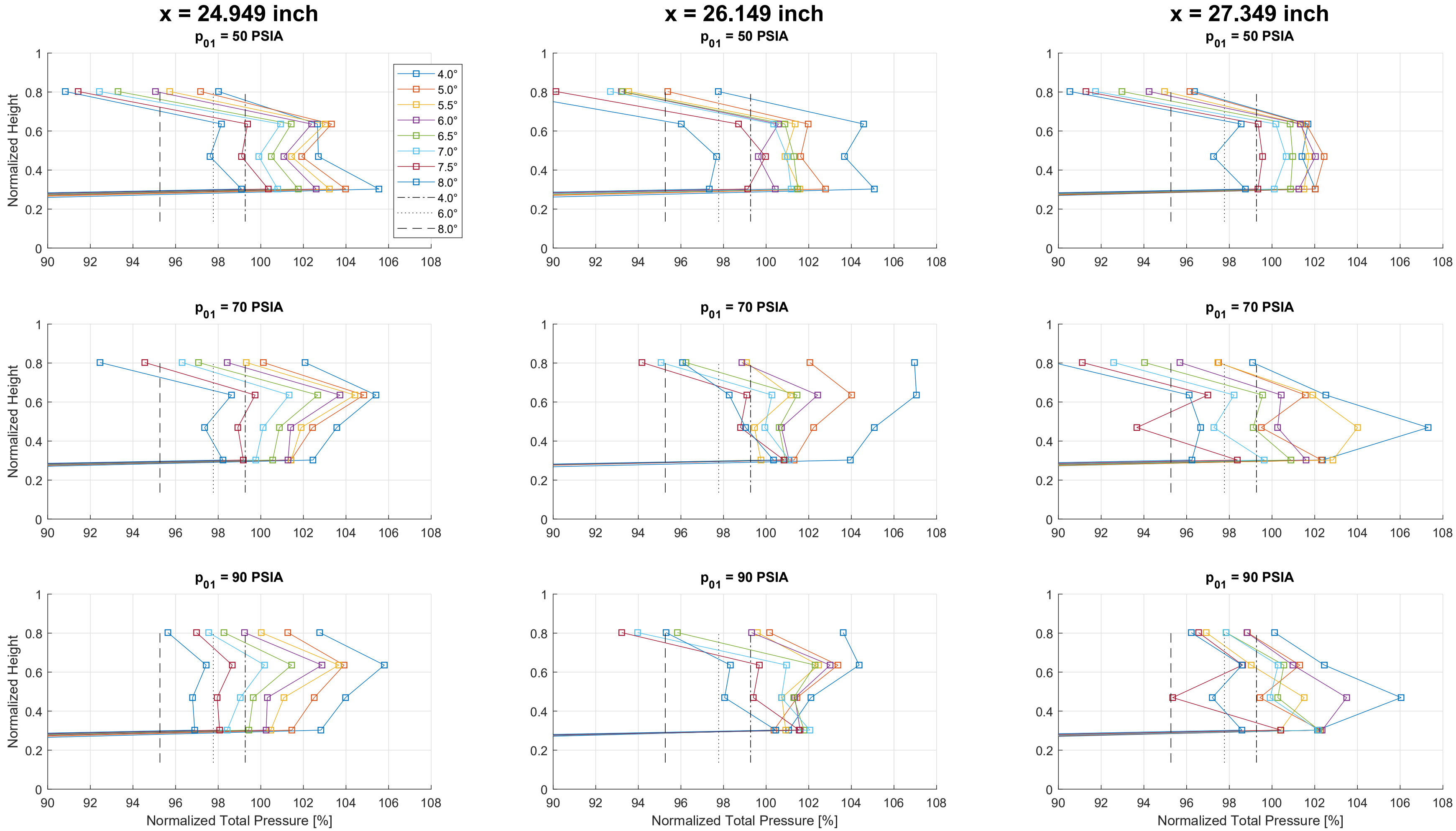

Fig. 37 Centerline total pressure profile (calculated) as function of plate angle, axial station and tunnel total pressure (50–90 psia). Pressure and height normalized by p_{01} and h, respectively.

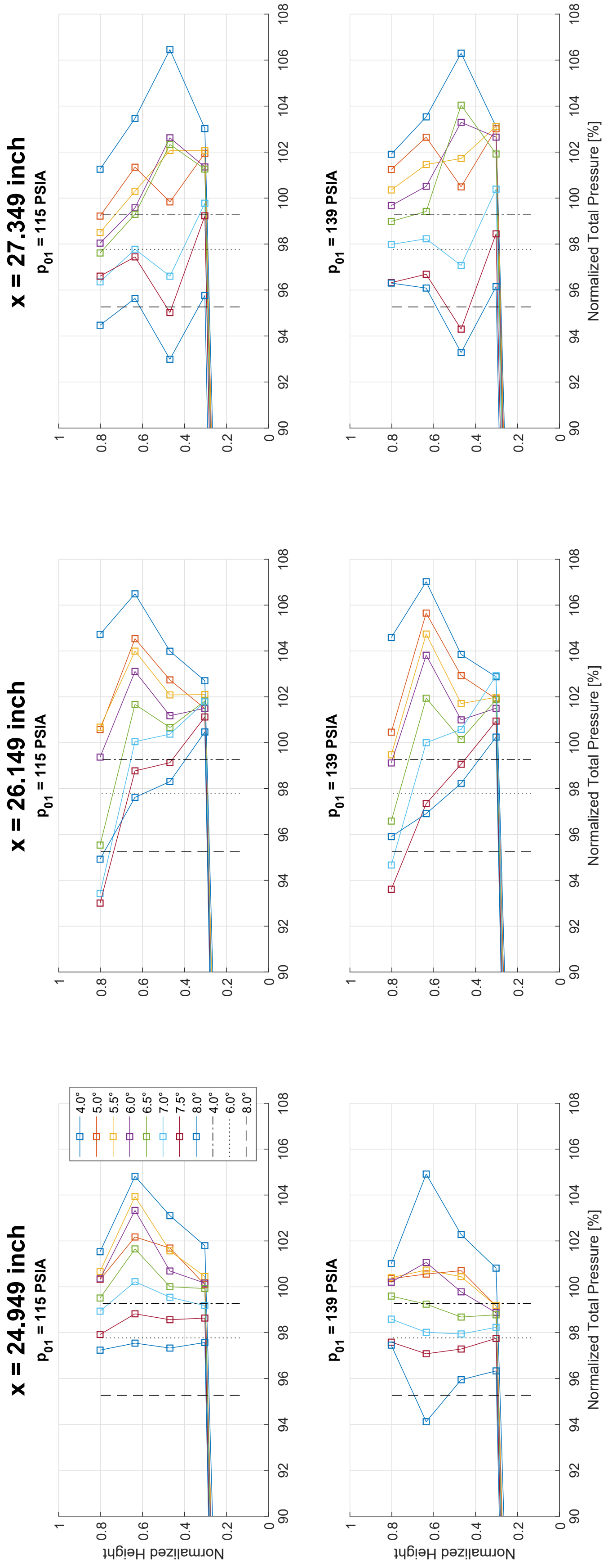

Fig. 38 Centerline total pressure profile (calculated) as function of plate angle, axial station and tunnel total pressure (115–139 psia). Pressure and height normalized by p_{01} and h, respectively.

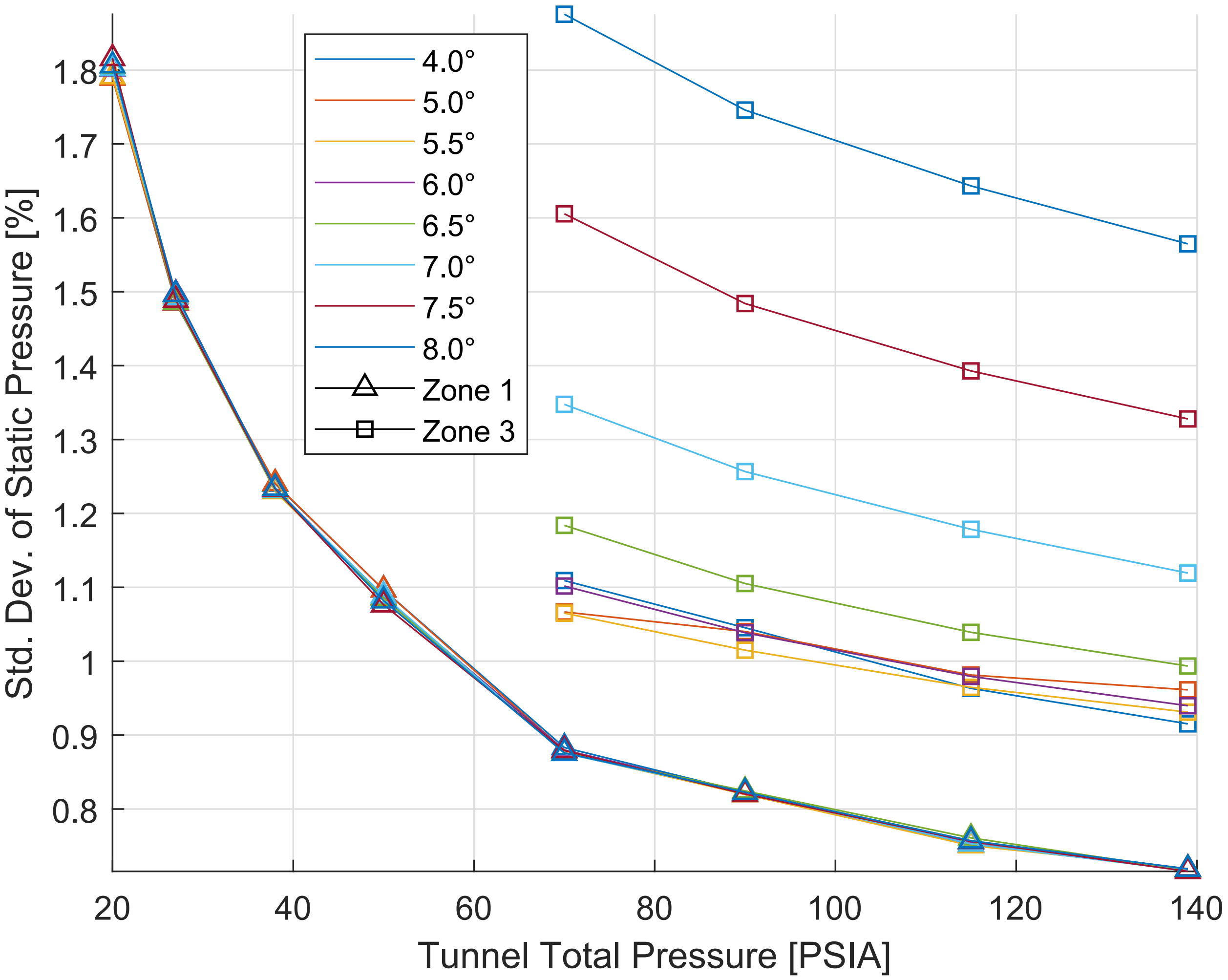

Fig. 39 Temporal standard deviation of surface static pressure along centerline in Zones 1 and 3 as function of plate angle and tunnel total pressure. Standard deviation normalized by temporal mean.